

Mitochondria-Targeting Click-Derived Pyridinyltriazolylmethylquinoxaline-Based Y-Shaped Binuclear Luminescent Ruthenium(II) and Iridium(III) Complexes as Cancer Theranostic Agents

Nilmadhab Roy,[†] Utsav Sen,[†] Yukti Madaan, Venkatesan Muthukumar, Seshu Varddhan, Suban K. Sahoo, Debashis Panda, Bipasha Bose,* and Priyanka Paira*

Cite This: <https://dx.doi.org/10.1021/acs.inorgchem.0c02928>

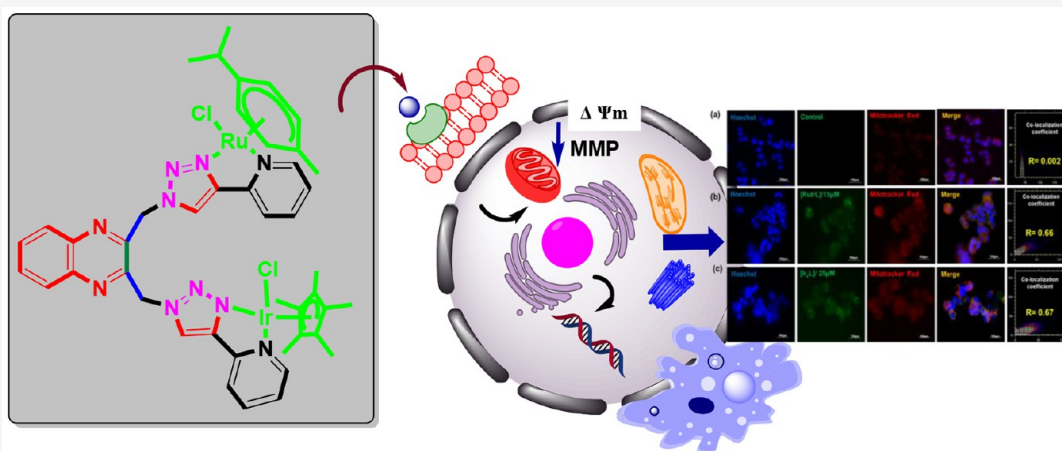
Read Online

ACCESS |

Metrics & More

Article Recommendations

Supporting Information



ABSTRACT: Due to several negative issues, market available drugs have been gradually losing their importance in the treatment of cancer. With a view to discover suitable drugs capable of diagnosing as well as inhibiting the growth of cancer cells, we have aspired to develop a group of theranostic metal complexes which will be (i) target specific, (ii) cytoselective, thus rendering the normal cell unaffected, (iii) water-soluble, (iv) cancer cell permeable, and (v) luminescent, being beneficial for healing the cancer eternally. Therefore, to reach our goal, we have prepared novel Ru(II)- and Ir(III)-based bimetallic and hetero bimetallic scaffolds using click-derived pyridinyltriazolylmethylquinoxaline ligands followed by metal coordination. Most of the compounds have displayed significant cytoselectivity against colorectal adenocarcinoma (Caco-2) and epitheloid cervical carcinoma (HeLa) cells with respect to normal human embryonic kidney cells (HEK-293) compared to cisplatin [*cis*-diamminedichloroplatinum(II)] along with excellent binding efficacy with DNA as well as serum albumin. Complex [$(\eta^6\text{-}p\text{-cymene})(\eta^5\text{-Cp}^*)\text{Ru}^{\text{II}}\text{Ir}^{\text{III}}\text{Cl}_2(\text{K}^2\text{-N,N-L})](\text{PF}_6)_2$ [**RuIrL**] exhibited the best cytoselectivity against all the human cancer cells and was identified as the most significant cancer theranostic agent in terms of potency, selectivity, and fluorescence quantum yield. Investigation of the localization of complex [**Ir₂L**] and [**RuIrL**] in the more aggressive colorectal adenocarcinoma cell HT-29 indicates that mitochondria are the key cellular target for destroying cancer cells. Mitochondrial dysfunction and G2/M phase cell cycle arrest in HT-29 cell were found to be involved in the apoptotic cell death pathway induced by the test complexes [**Ir₂L**] and [**RuIrL**]. These results validate the concept that these types of complexes will be reasonably able to exert great potential for tumor diagnosis as well as therapy in the near future.

INTRODUCTION

The great menace of cancer as the second most lethal disease in developing countries has created a perilous situation in the living world where medical science is still incapable of finding out appropriate medicines to abate its rampant proliferation.^{1,2}

The urgent development of an efficient anticancer drug is, therefore, long awaited, which could be accomplished by the means of advanced technology and improved conception in

Received: October 1, 2020

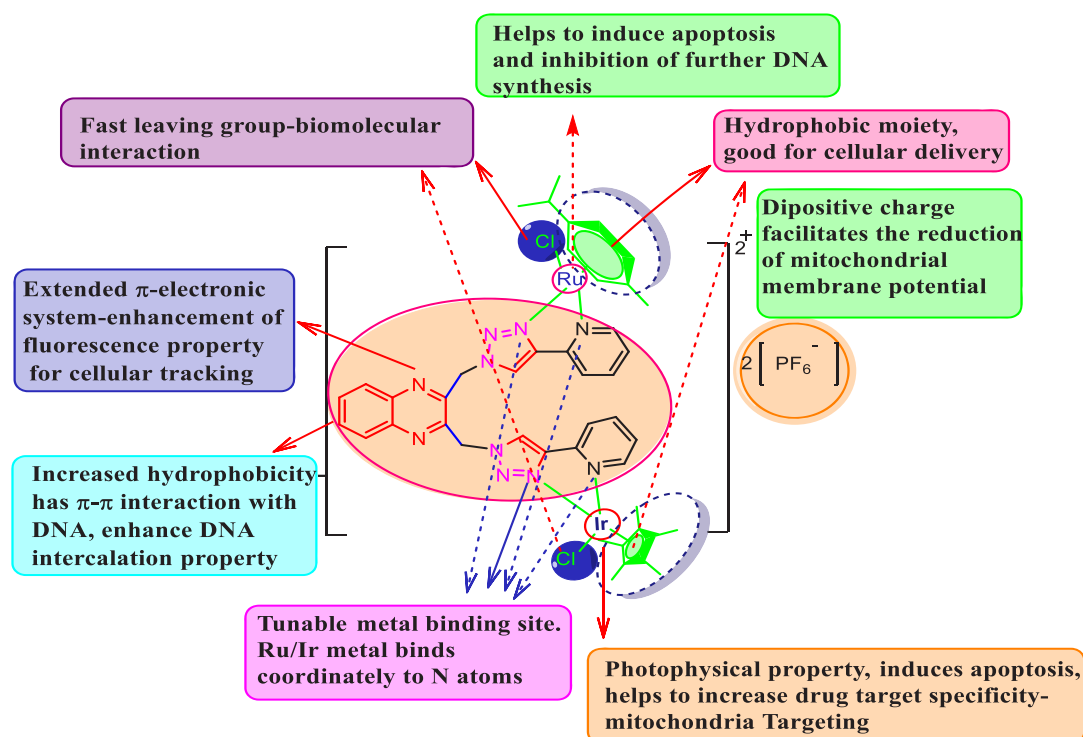
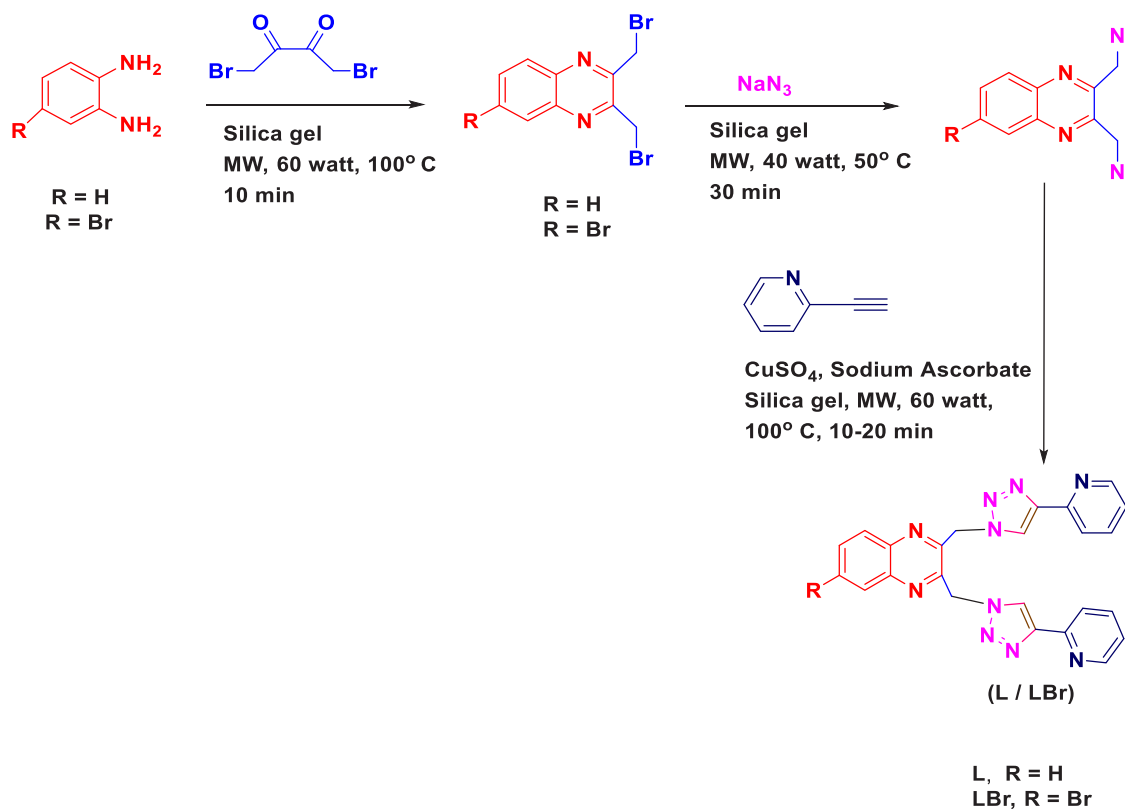


Figure 1. Design of pyridinyltriazolylmethylquinoxaline-based binuclear luminescent Ru(II) and Ir(III) complexes.

cancer biology, the consequences of which led to the discovery of *cis*-diamminedichloroplatinum(II) (cisplatin) by Rosenberg in 1965, inaugurating the new era of anticancer research based on metallopharmaceuticals.³ The major concerns with cisplatin, aside from its restricted scope of action, are its high toxicity as well as its proclivity in creating tumor resistance in patients.^{4,5} Eventually, all these short comings compelled researchers to think of a new way for designing an outstanding drug alternative to cisplatin having lower toxicity and less issues with tumor resistance along with a broader spectrum of activity.^{6,7} In this regard, ruthenium(II) and iridium(III) complexes are undeniably the most superb candidates among potential anticancer metallodrugs other than platinum-based complexes. Their inherent properties like activity against cisplatin resistant various cell lines, lower side effects, less toxicity to healthy cells for being highly selective toward cancer cells,⁸ greater affinity to subcellular target (a particular organelle), the ability of ruthenium to mimic iron in binding to various biological molecules,⁸ redox accessible oxidation states, water tolerance,⁹ and relatively low reduction potential¹⁰ have wonderfully boosted their capability to act as anticancer metallodrugs. Keen interest in designing ruthenium-based anticancer drugs has been mounting rapidly since KP1019 and after that its sodium salt, KP1339, have effectively completed phase I clinical trials and are in the process to enter phase-2 clinical trials in the near future.^{11–15} Other remarkable success were observed for Ru(II) metallotherapeutics such as TLD1433, which has entered phase-1 and phase-2a clinical trials with photodynamic therapy (PDT) for nonmuscle invasive bladder cancer treatment.¹⁶ Many researchers have successfully discovered various types of novel Ru(II) scaffolds which have been investigated up to preclinical studies. As an example, the Ru-PTA (1,3,5-triaza-7-phosphaadamantane) complex RAPTA-C,¹⁷ along with Erlotinib, has exhibited proficient anticancer activity. In

addition to this, more advancement on patents of ruthenium complexes with various scaffolds has also been reported.^{18–25} RAED44, a ruthenium-based compound with a 1,2-ethylenediamine ligand was reported to have the ability of binding to DNA *in vitro* neoplastic cells²⁶ and to form adducts with guanine. DW1/2²⁷ is the first ruthenium based antitumor agent targeting through a signal transduction pathway. In 2004, a new class of RAPTAs bearing phosphoadamantane and arene ligands were reported as anticancer agents. For example, [Ru(η^6 -*p*-cymene)Cl(2)(pta)], (RAPTA-C)²⁸ and Ru(η^6 -C₆H₅Me)-(pta)Cl₂ (RAPTA-T) are well-known.²⁹ A group of researchers have been able to develop a number of cationic biscyclometalated Ir(III)-based metal complexes as marvelous cellular imaging agents which becomes possible only by the means of some fantastic features of Ir(III) organometallic compounds. These are (i) large Stokes shifts (>100 nm) to avoid inner filter effects, (ii) rapid transmembrane activity (short incubation time and less potential toxicity), (iii) long luminescence lifetimes (100 ns) for time-resolved detection, and (iv) enhanced photostabilities (less photobleaching) when used in the imaging process. Moreover, a number of Ir(III) complexes have recently been explored as anticancer as well as cancer theranostic agents, and Ir(III) cyclometalated complexes have also appeared as effective photodynamic therapeutic agents. Recently, Peter J. Sadler, an eminent inventor of various organometallic compounds from the University of Warwick,³⁰ obtained patents on the application of organometallic iridium-based anticancer complexes with the aid of the most modern concepts in the field of metallodrugs. The aforementioned complexes displayed dual properties of killing cancer cells via DNA damage and simultaneously by mitochondrial dysfunction by ROS production along with detection of cancer cells in the human body. Mitochondria have been deliberated as potential cellular O₂ sensors and also play a significant role in cellular metabolism by activating the

Scheme 1. Click-Derived Pyridinyltriazolylmethylquinoxaline ligand (L/LBr) Synthesis⁴⁹

extrinsic and intrinsic apoptotic pathways.³¹ Therefore, mitochondria have been taken into consideration as a prime target for cancer cell annihilation. The intrinsic phosphorescence property of Ir(III) complexes can be used to track drug delivery in the body and monitor the accumulation of a drug in subcellular organelles, which assists with the optimization therapy and finding the mechanism of cell death.³² In the extracellular medium, the metabolic pathways take part in competition among the aquation, reduction, and hydrolysis after binding to transport proteins and cell-surface biomolecules and after that the ability of diffusion into the cells. The extent to which each drug participates in these steps along with the focused pathways is very crucial in determining whether the drug is mainly antimetastatic or cytotoxic.

Quinoxaline derivatives have already been recognized for their biological activities and are significant in the pharmaceutical industry having antimicrobial,³³ antiviral,³⁴ antituberculosis,³⁵ anti-inflammatory,^{36,37} and anticancer activities.³⁸ Furthermore, “click chemistry” is being used to have a pronounced imprint in material science,^{39–41} especially in building up the novel structures of polymers^{42,43} and dendrimers.⁴⁴ The unique template “triazole” has also been concomitant with quinoxaline moieties being associated with antifungal, antibacterial, antiviral, antitumor, antimicrobial, antitubercular, anti-inflammatory, antimalarial, anti-HIV, cardiovascular, and also CNS activities.^{45–48} Therefore, our prime objective of this project is to synthesize a group of ligands possessing bistriazole and quinoxaline moieties in a single domain and their further exploration into multinuclear complexes. Since both the ligand and the metal centers are acquaintance with their selectivity as well as specificity in anticancer action, the idea of developing significant cytoselectivity and targeting specific binuclear Ru(II) and Ir(III)

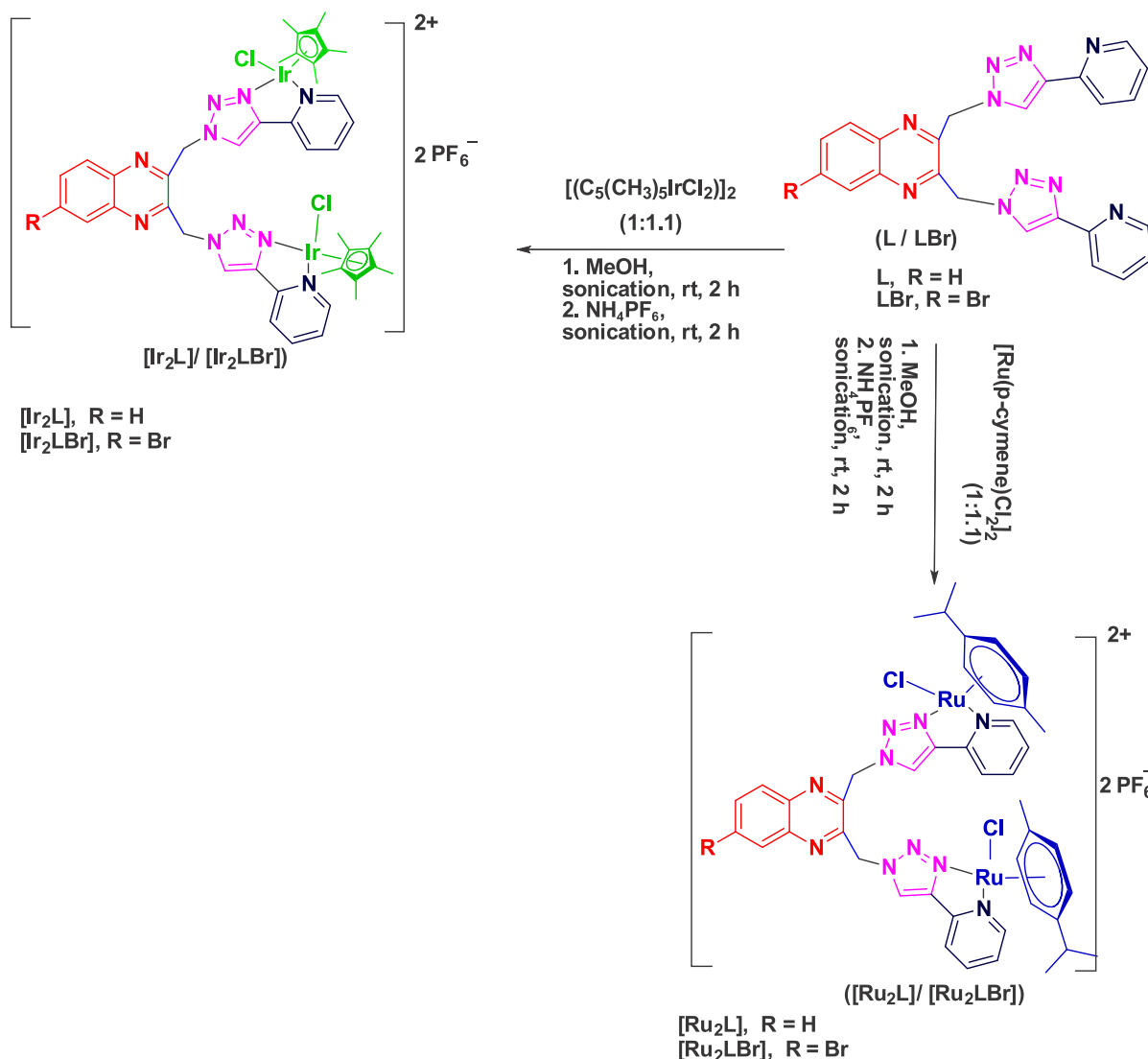
complexes were on our mind to bring forth novel anticancer metallo drugs that will be competent in showing the combined properties of two different metals in the same scaffold (Figure 1).

RESULTS AND DISCUSSION

Chemistry. Synthesis and Characterization. Syntheses of ligands L and LBr and their respective complexes with Ru(II) and Ir(III) [Ru_2L], [Ru_2LBr], [Ir_2L], [Ir_2LBr], [RuL], [IrL], and [RuIrL] have been summarized in Schemes 1, 2, and 3. At the outset, *o*-phenylenediamine derivatives and 1,4 dibromo-2,3-butanedione were supported on silica and then irradiated under microwave for 10 min at 100 °C (Scheme 1).⁴⁹ After completion of the reaction, silica gel was thoroughly washed with ethanol followed by slow evaporation to get the gray crystals of bis(bromomethyl)quinoxaline. The conversion of bromide to azide was accomplished by the reaction of silica supported mixture of bis(bromomethyl)quinoxaline and sodium azide under microwave condition. Then ligands L and LBr were prepared following the click chemistry protocol briefly by the treatment of silica supported 2,3-bis-(azidomethyl)quinoxaline with 2-ethynylpyridine for 10–20 min. The crude triazoles were further recrystallized with hexane-ethyl acetate (1:1) mixture and brown crystalline ligands (L or LBr) were obtained with high yields. The ligands L and LBr were then analyzed by ¹H and ¹³C NMR, IR, and mass spectroscopy.⁴⁹

In ¹H NMR spectrum of 2,3-bis(bromomethyl)quinoxaline, the most downfield two protons near to the nitrogen atoms appeared as double doublet (dd) at δ 8.07 ppm. The other two aromatic protons were observed at δ 7.79 ppm as a double doublet and last four aliphatic CH₂ protons were observed as singlet peak at δ 4.93 ppm. In ¹³C NMR spectrum, the most

Scheme 2. One Pot Synthesis of Binuclear Ru(II) and Ir(III) Pyridinyltriazolymethylquinoxaline Complexes

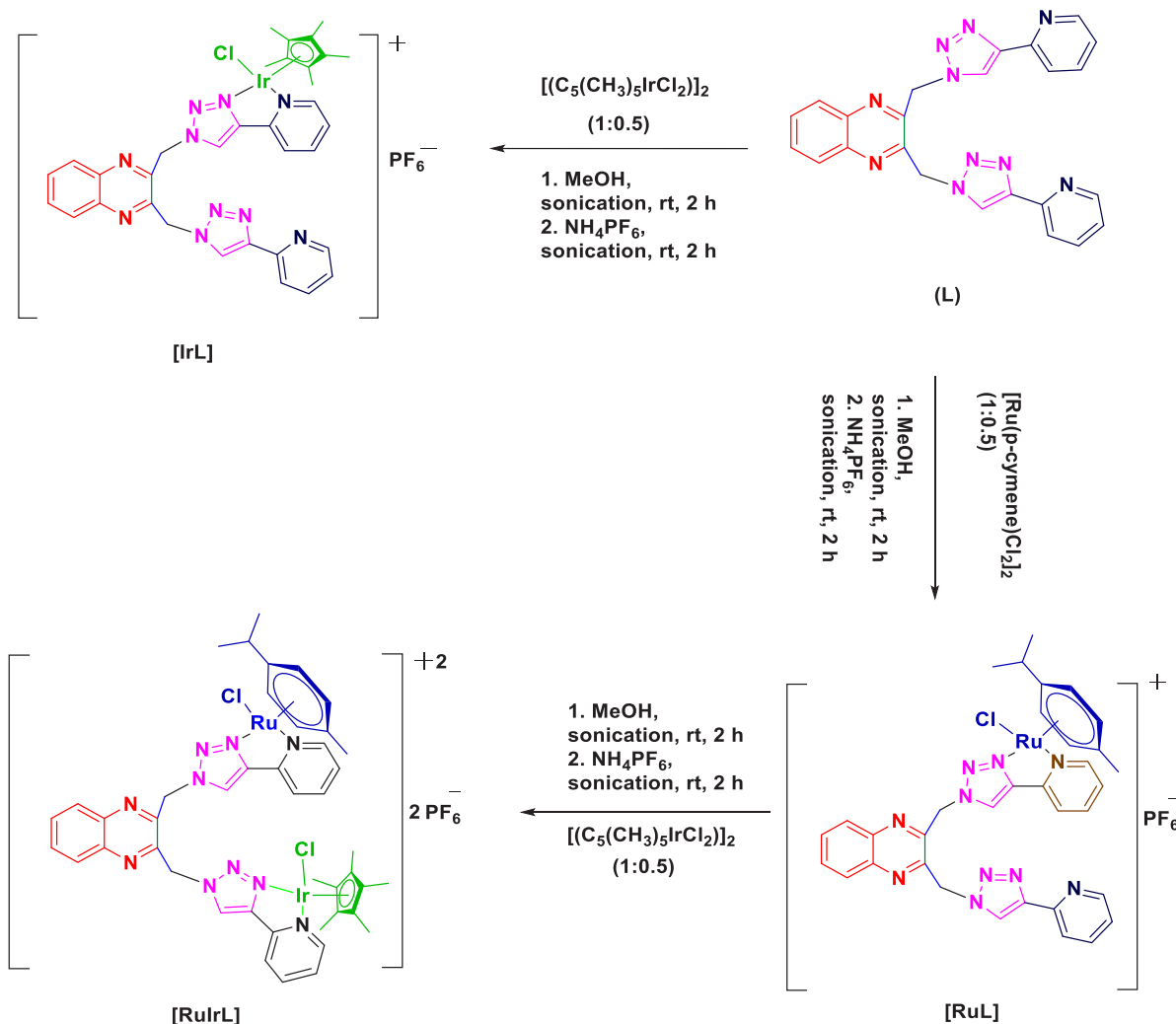


characteristic peaks of CH_2 were found at δ 30.49 ppm. There were no significant differences observed in 1H NMR spectra of azidomethylquinoxaline and bromomethylquinoxaline. In the ^{13}C NMR spectra, most characteristic peaks of CH_2 of compounds 2,3-bis(azidomethyl)quinoxaline and 2,3-bis(azidomethyl)-6-bromoquinoxaline were observed at δ 52–53 ppm because of the presence of the azide group. The characteristic peaks of $N=N=N$ stretching of these compounds were displayed at 2083 and 2094 cm^{-1} in the IR spectra. In the 1H NMR spectrum of compound L, the most downfield two protons adjacent to the two nitrogen atoms of pyridine appeared as a broad singlet at δ 8.56 ppm. The characteristic singlet peak of aromatic proton present in triazole was observed at δ 8.38 ppm. The remaining aromatic protons of pyridine rings and quinoxaline ring were observed in the range of δ 7.76–8.18 ppm. Lastly, the characteristic four aliphatic CH_2 protons were recorded as singlet at δ 6.16 ppm. In ESI-MS, the characteristic molecular ion peak of compound L was observed as $[M + H]^+$, 447.4. The complexes $[Ru_2L]$, $[Ru_2LBr]$ and $[Ir_2L]$, $[Ir_2LBr]$ were formed by chloro bridge cleavage of $[(\eta^6-p-cymene)RuCl(\mu-Cl)]_2$ and $[(\eta^5-Cp^*)IrCl(\mu-Cl)]_2$ respectively with the reaction of ligands L, LBr (Scheme 2). Herein, the alcoholic solutions of metal

precursors were treated with ligands (L, LBr) under sonication for 2 h at ambient temperature. The progress of the reactions was monitored by TLC. In order to facilitate anion exchange, solid NH_4PF_6 was added to the reaction mixture and again sonicated for 2 h at ambient temperature. The solvent was evaporated after completion of the reactions, and brown powderlike crude products were obtained. Then the crude products were washed thoroughly with hexane and recrystallized from diethyl ether/methanol mixture to remove the impurities. At last, brown needle-shaped crystals of Ru(II) complexes $[Ru_2L]$, $[Ru_2LBr]$ and dark yellow fine crystals of Ir(III) complexes $[Ir_2L]$, $[Ir_2LBr]$ were obtained with high yields (90–95%). The structures of all these complexes were analyzed by 1H , ^{13}C , ^{19}F , and ^{31}P NMR, FT-IR, and HRMS.

In the 1H NMR spectrum, the protons of the ligand were shifted to more downfield in case of Ru(II) binuclear complex, $[Ru_2L]$. For example, the peaks of L in the region of δ 7.26–8.56 ppm were moved to δ 7.71–9.53 ppm in the complex, $[Ru_2L]$. The four aliphatic CH_2 protons which were displayed in L at δ 6.15 ppm as a singlet were changed to two doublets in the region of 6.61–6.75 ppm in the complex. The two sets of methyl protons of the *p*-cymene ring were observed in the range of δ 1.00–1.09 ppm, as two distinct doublets. The six

Scheme 3. Synthesis of Ru(II) and Ir(III) Pyridinyltriazolylmethylquinoxaline Monometallic and Mixed Metallic Complexes



protons of another two methyl groups appeared as singlet at δ 2.17 ppm. Similarly, CH protons of the isopropyl groups were found as multiplet in the region of δ 2.62–2.69 ppm. The eight aromatic protons of *p*-cymene rings were appeared in the region of δ 5.86–6.18 ppm. The characteristic phosphorus and fluorine peaks in ^{31}P and ^{19}F NMR spectra were observed in the region of δ –153.04 to –135.47 ppm and δ –71.01 ppm, respectively. The P–F stretching at 829 cm^{-1} , $\text{sp}^3\text{ C–H}$ stretching at 2970 cm^{-1} and $\text{sp}^3\text{ C–H}$ bending at 1442 and 1404 cm^{-1} were observed in the IR spectrum which indicated the existence of PF_6^- in Ru(II) complex. The HRMS peak at m/z : 494.0699 $[\text{M} - 2\text{PF}_6]^{2+}$ confirmed the formation of the complex $[\text{Ru}_2\text{L}]$. The Ir(III) binuclear complex $[\text{Ir}_2\text{L}]$ was fully characterized by ^1H , ^{13}C , ^{19}F , and ^{31}P NMR, FT-IR, and HRMS. Similarly, in complex $[\text{Ir}_2\text{L}]$, the splitting patterns of all the protons of ligands were moved toward the downfield region. The four aliphatic CH_2 protons were displayed in L as a singlet at δ 6.16 ppm changed to δ 6.69 ppm in the complex. The ligand protons present in the complex were exhibited in the range of δ 7.76–9.45 ppm. The most characteristic 30 Cp^* protons appeared as a singlet at δ 1.73 ppm. The characteristic phosphorus and fluorine peaks of PF_6^- were observed in the region of δ –153.00 to –135.44 ppm and –71.06 to –69.17 ppm, respectively. In the ^{13}C NMR spectrum, the characteristic methyl carbon peaks and singlet carbons of the Cp^* moiety

were observed in the range of δ 8.7–9.0 ppm and 89.4–92.6 ppm, respectively. The appearance of P–F stretching at 827 cm^{-1} , $\text{sp}^3\text{ C–H}$ stretching at 3037 cm^{-1} , and $\text{sp}^3\text{ C–H}$ bending at 1423 cm^{-1} in the IR spectrum indicated the existence of PF_6^- in Ir(III) complex. The HRMS peak at m/z : 586.1349 $[\text{M} - 2\text{PF}_6]^{2+}$, confirmed the formation of complex $[\text{Ir}_2\text{L}]$.

The Ru(II) mononuclear complex $[\text{RuL}]$ was prepared by the treatment of $[(\eta^6\text{-p-cymene})\text{RuCl}(\mu\text{-Cl})_2]$ in methanol with the ligand L (1:2 equiv) under sonication for 2 h. After a change in color from deep yellow to brown, 2.1 equiv of NH_4PF_6 was added to the reaction medium and sonicated for another 2 h. The Ir(III) mononuclear complex $[\text{IrL}]$ was also prepared in a similar fashion. Furthermore, the Ru(II) and Ir(III) mixed metal complex $[\text{RuIrL}]$ was prepared by treating $[(\eta^5\text{-Cp}^*)\text{IrCl}(\mu\text{-Cl})_2]$ with complex $[\text{RuL}]$ in (1:2 equiv) methanol under sonication for 2 h. After complete conversion to the product, ligand exchange was performed with the addition of NH_4PF_6 to the reaction medium in a similar manner (Scheme 3). The complexes $[\text{RuL}]$, $[\text{IrL}]$, and $[\text{RuIrL}]$ were fully characterized by ^1H and ^{13}C NMR, IR, and HRMS. The characteristic doublet peaks of two methyl protons of *p*-cymene in complex $[\text{RuL}]$ were observed at δ 1.01–1.09 ppm whereas other methyl protons appeared as a singlet at δ 2.18 ppm. The characteristic multiplet peaks of CH protons were observed in the range of δ 2.63–2.67 ppm.

Table 1. Photophysical Characterization, Solubility, Lipophilicity, and Conductivity Study of the Complexes [Ru₂L], [Ru₂LBr], [Ir₂L], [Ir₂LBr], and [RuIrL]

complexes	λ_{\max} (nm) ^a	λ_f (nm) ^b	Stoke's shift	OD ^c	ϵ (M ⁻¹ cm ⁻¹) ^d	(ϕ_f) ^e	solubility (M) ^f	log <i>P</i> ^g	Λ_M^h (S cm ² mol ⁻¹)	
									DMSO	10% DMSO
[Ru ₂ L]	260, 300, 335	380, 450	60, 130	0.48	16000	0.28	0.032	0.20 ± 0.01	132	300
[Ru ₂ LBr]	260, 300, 335	378, 450	53, 125	0.51	17000	0.16	0.029	0.45 ± 0.03	–	–
[Ir ₂ L]	260, 300, 340	415, 450, 500	90, 125, 175	0.32	10667	0.43	0.030	0.27 ± 0.05	140	420
[Ir ₂ LBr]	260, 300, 345	384, 450, 496	54, 120, 166	0.56	18667	0.21	0.026	0.11 ± 0.01	–	–
[RuIrL]	260, 290, 330	380, 515	55, 190	0.35	11667	0.46	0.019	0.96 ± 0.02	136	350
cisplatin	200, 300	–	–	0.26	8667	–	0.017	–	34	213
quinine sulfate	350	452	102	0.08	2667	0.546	–	–	–	–

^aAbsorption maxima. ^bMaximum emission wavelength (λ_{exc} 325–330 nm). ^cOptical density. ^dExtinction coefficient. ^eQuantum yield. ^fDMSO–10% DMEM medium (1:99 v/v, comparable to cell media). ^g*n*-Octanol/water partition coefficients. ^hConductance in DMSO and 10% aqueous DMSO (complex concentration 3×10^{-5} M).

Likewise, the characteristic 15 Cp* protons of complex [IrL] were appeared as singlet at δ 1.73 ppm. The HRMS peaks of complex [RuL] and complex [IrL] appeared at *m/z*: 717.1552 [M – PF₆]⁺ and 809.2205 [M – PF₆]⁺, respectively. In the case of mixed metallic complex [RuIrL], the characteristic 15 Cp* protons were recorded as a singlet at δ 1.73 ppm, and the methyl protons of *p*-cymene appeared as singlet at δ 2.18 ppm and two doublets in the region of δ 1.00–1.09 ppm. The characteristic CH protons of the isopropyl group were observed as multiplet at δ 2.62–2.67 ppm. The HRMS peak at *m/z* 540.1012 [M – 2PF₆]²⁺ confirmed the formation of the complex [RuIrL].

Electronic Absorption (UV–Visible) and Fluorescence Study. To emphasize the cellular imaging properties of the synthesized complexes [Ru₂L], [Ru₂LBr], [Ir₂L], [Ir₂LBr], and [RuIrL], UV and fluorescence studies were conducted in (1:9, v/v) dimethyl sulfoxide (DMSO): water mixture (Figure S1 and S2). These complexes exhibited strong absorption peaks in the range of 260–300 nm due to characteristic intraligand (NAN ligands) transitions (LLCT) and lower energy broad absorption bands in the range of 320–450 nm due to metal to ligand charge transfer (MLCT).^{50,51} The absorption peak at the lower wavelength region appeared due to the charge transfer between the π -bonding molecular orbital of ligand (HOMO) to the π^* -antibonding molecular orbital (LUMO), i.e., due to π – π^* transition, and the appearance of a less intense absorption band at a higher wavelength region was due to charge transfer from the metal's low lying filled d-orbital (*t*_{2g}) to the vacant higher energy antibonding π^* molecular orbitals of the ligands which was regarded as a MLCT transition. The complexes showed emission in the range of 350–600 nm for MLCT by the electronic transition from ligand π^* molecular orbital to metal *t*_{2g} orbital. The corresponding quantum yields (Φ_f) of these complexes were calculated from the emission spectral data, which could be used for photocytotoxicity and cellular imaging purposes (equation ii, Table 1). It was evident that all the compounds were significantly fluorescent, and compound [RuIrL] showed the highest quantum yield (Φ_f), about 0.46 in 10% DMSO medium, among them.

Solubility, Lipophilicity, and Conductivity Study. The tumor-inhibiting potential of metal complexes is strongly dependent on the equilibrium between hydrophilicity and lipophilicity. These bimetallic or mixed metallic complexes are highly soluble in DMSO and DMF and had moderate to good solubility in H₂O, MeOH, EtOH, CH₃CN and poor solubility

in hydrocarbon solvents. It is noteworthy to mention that these complexes are soluble in the range of 5–8 mg per mL of DMSO–10% DMEM medium (1:99 v/v, comparable to cell media) at 25 °C. To know the lipophilic properties or drug-like behavior of these complexes [Ru₂L], [Ru₂LBr], [Ir₂L], [Ir₂LBr], and [RuIrL], we had estimated the *n*-octanol/water partition coefficient ($\log P_{o/w}$ where $P_{o/w}$ = the octanol/water partition coefficient), using the shake flask method (Figure S3 and Table 1).^{52–54} The experimental $\log P_{o/w}$ values of these complexes were obtained in the range 0.11–0.96. Complex, [RuIrL] exhibited highest order of $\log P_{o/w}$ due to the lipophilic character of *p*-cymene, Cp* and iridium metal which supported the significant mitochondrial accumulation. The bimetallic [Ru₂L], [Ir₂L], and heterobimetallic [RuIrL] complexes displayed the molar conductance values of 132, 140, and 136 S cm² mol⁻¹ respectively in pure DMSO suggesting their 1:2 electrolytic nature.⁵⁵ Agreeably, the molar conductance of all these complexes were significantly increased in 10% aqueous DMSO (~300–420 S cm² mol⁻¹, Table 1), proposing their 1:4 electrolytic nature. Thus, the obtained conductivity of these complexes attributed to the dissociation of the M–Cl bond in the tested system and confirmed the ionization of complexes in aqueous medium which ensured significant binding properties of complexes with biomolecules. Moreover, the conductance values of these complexes were increased gradually with time up to 6 h after incubation in 10% DMSO suggesting the easiness of departure of the labile –Cl group from the complexes (Figure S4). On the other hand, cisplatin exhibited poor conductance ($\Lambda_M = 34$ S cm² mol⁻¹) in DMSO and showed 1:2 electrolytic property ($\Lambda_M = 213$ S cm² mol⁻¹) in 10% DMSO.

Stability Study of the Complexes by UV–Vis Spectroscopy. The stability study of the three complexes, namely [Ru₂L], [Ir₂L], and [RuIrL], was accomplished in two mediums, 1% DMSO in water and GSH (1 mM) medium. This study was needed to determine the stability of complexes in the biological environment inside the cell so as to be a potent therapeutic agent. A reasonable change in the UV–vis spectral profile with the λ_{\max} value over 48 h in 1% DMSO was observed for each complex, suggesting that M–Cl bond was moderately stable in less water content (Figure S5). Such change in absorption bands indicates that these complexes can easily form aqua complexes in bulk water medium, which can also be quantitatively justified by the observed molar conductivity of the respective complexes in aqueous DMSO.⁵⁶ Moreover, the ¹H NMR study in 10% DMSO/

D₂O mixture did not show any change in spectral pattern suggesting no dissociation of the ligands from the complexes (Figure S6). It is well-known that glutathione (GSH) is a crucial detoxifying agent in the presence of glutathione S-transferase (GST) in cells.^{57,58} Henceforth, to see the activity of GSH on these complexes, [Ru₂L], [Ir₂L], and [RuIrL], the stability study was performed in the presence of excess (10 equiv) glutathione by time dependent UV-vis spectroscopy which displayed minor changes in absorbance with time (Figure S7), i.e., complexes were not being deactivated by GSH. Biomolecules can exhibit the binding affinity with the metal complexes and therefore a competitive binding between GSH and serum albumin with the complex may be started to prevail when drug enters into the cell.^{56,59,60} But, in our case, as GSH was incompetent to bind with these complexes, binding with serum albumin will prevail when the drug will enter into the cell, ruling out the probability of competitive binding, which has been further justified from the binding study with the serum albumin in the later section.

Electrochemical Properties. In order to get some insights into the stability of the Ru(II) and Ir(III) state in these complexes, the electrochemical behavior of the reported complexes were studied with the aid of cyclic voltammetry at a fixed scan rate. Figure 2 represents a cyclic voltammetric

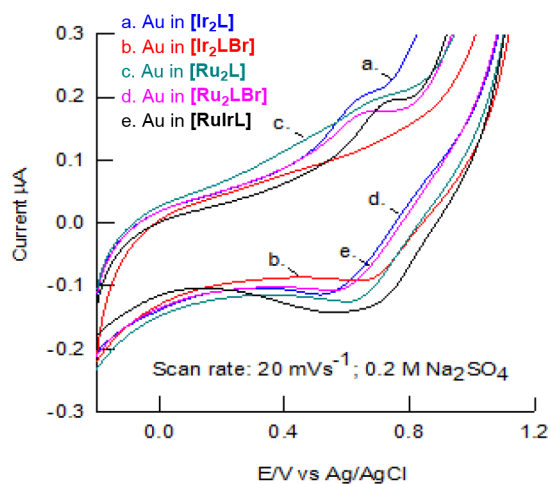


Figure 2. Cyclic voltammetry response of the samples at the potential window of -0.2 to 1.2 V vs Ag/AgCl in 0.2 M of sodium sulfate solution at scan rate of 20 mV s⁻¹.

response of various Ru and Ir complexes in 0.2 M Na₂SO₄ medium (10 mL) with 0.5 mL of ethanol at a scan rate, 20 mV s⁻¹. On the basis of the magnitude of anodic (i_{pa}) and cathodic peak (i_{pc}) currents, it had been found that complex [Ir₂LBr] showed an irreversible electrochemical behavior ($i_{pa} \ll i_{pc}$), whereas, other complexes displayed well-defined reversible redox peak ($i_{pa} \cong i_{pc}$) with an apparent standard electrode potential, $E^{o'} = 0.600 \pm 0.50$ V vs Ag/AgCl, which was closer to the literature value, 0.55 V vs Ag/AgCl in neutral pH solution.⁶¹ The detailed information for the $E^{o'}$ values of all the complexes have been provided in Table S1. On the basis of obtained electrode potential values, we can depict that the possible redox-state of these metal complexes will be Ru(III)/Ru(II) and Ir(III)/Ir(II). This observation nicely described the electroactive functionality of the synthesized complexes in aqueous medium.

Theoretical Study. Computational Study. The density functional theory (DFT) method was applied to compute the probable 3D structure of the metal complexes. All calculations were performed in the gas phase by using the B3LYP exchange-correlation functional and the basis sets LANL2DZ for Ru and Ir atoms whereas 6-31G** for the remaining atoms. The computational programs Gaussian 09W and Gauss View were used for the calculations.⁶² The computed structures of the Y-shaped half-sandwich organometallic complexes were shown in Figure 3. The quinoxaline unit separated the two metal centers forming the half-sandwich complex by a methylene group that provided sufficient flexibility to form a perfect Y-shaped organometallics. Each metal center in the complexes formed a pseudo-octahedral coordination geometry, where the metal atom (Ir or Ru) was coordinating to all six carbon atoms of *p*-cymene ring in the case of Ru complexes whereas all five carbon atoms of pentamethylcyclopentadiene were coordinated in the case of Ir, along with a chloride ion and the two nitrogen atoms of the pyridine-N and triazole-N. The bond lengths and bond angles of the Ru complexes in [Ru₂L], [Ru₂LBr] and [RuIrL] and Ir complexes in [Ir₂L], [Ir₂LBr], and [RuIrL] are similar. Each metal center mimics the well-known familiar “three leg piano-stool” structure, where the seat is formed by the η^5 -/ η^6 -arene and the three legs of the stool are constituted by the pyridine-N and triazole-N atoms and the chloride ion. In complex [RuIrL], the observed bond angles for the triazole-N–Ru–Cl (83.79°) and pyridine-N–Ru–Cl (84.33°) in the Ru center and the bond angles for the triazole-N–Ir–Cl (84.31°) and pyridine-N–Ir–Cl (83.59°) in the Ir center are close to 90° supporting the “piano-stool” structure. The distance from the Ru center to the six carbons of the arene has almost identical bond lengths (2.252 – 2.337 Å) with an average distance of 2.292 Å. The triazole-N and pyridine-N atoms coordinated respectively to the Ru with the bond distance of 2.077 and 2.139 Å, where the triazole-N is coordinated more strongly than the pyridine-N. The calculated Ru–Cl bond length was obtained as 2.423 Å. Similar to Ru center, the distance from the Ir center to the five carbons of the arene have almost similar bond length (2.199 – 2.238 Å) with an average distance of 2.230 Å.

The triazole-N and pyridine-N atoms coordinated to the Ir with the bond distance of 2.104 and 2.147 Å, respectively, where the triazole-N is coordinated more strongly than the pyridine-N. The Ir–Cl bond length was obtained as 2.438 Å. Furthermore, to examine the changes in the electron densities distribution, the highest occupied molecular orbital (HOMO) and lowest unoccupied molecular orbital (LUMO) of L, [Ru₂L] and [Ir₂L] were drawn and compared (Figure 4). In case of L, the HOMO electron densities were distributed mainly over the pyridinyl–triazolyl unit whereas the LUMO electron densities were located over quinoxaline unit. Upon complexation with the Ir/Ru atom, the HOMO electron densities were mainly distributed around the metal center whereas the LUMO was over the quinoxaline unit. The band gap of L was decreased upon forming the complexes [Ru₂L] and [Ir₂L]. These results indicate that internal charge transfer occurred between the quinoxaline unit and the metal center. Similar distributions were observed in other organometallics.

Molecular Docking Study. To identify possible binding sites and mode of interactions of the complexes with the BSA (bovine serum albumin) and DNA, molecular docking experiments were performed to estimate the free energy of binding using the Autodock 4.2 by applying the Lamarckian

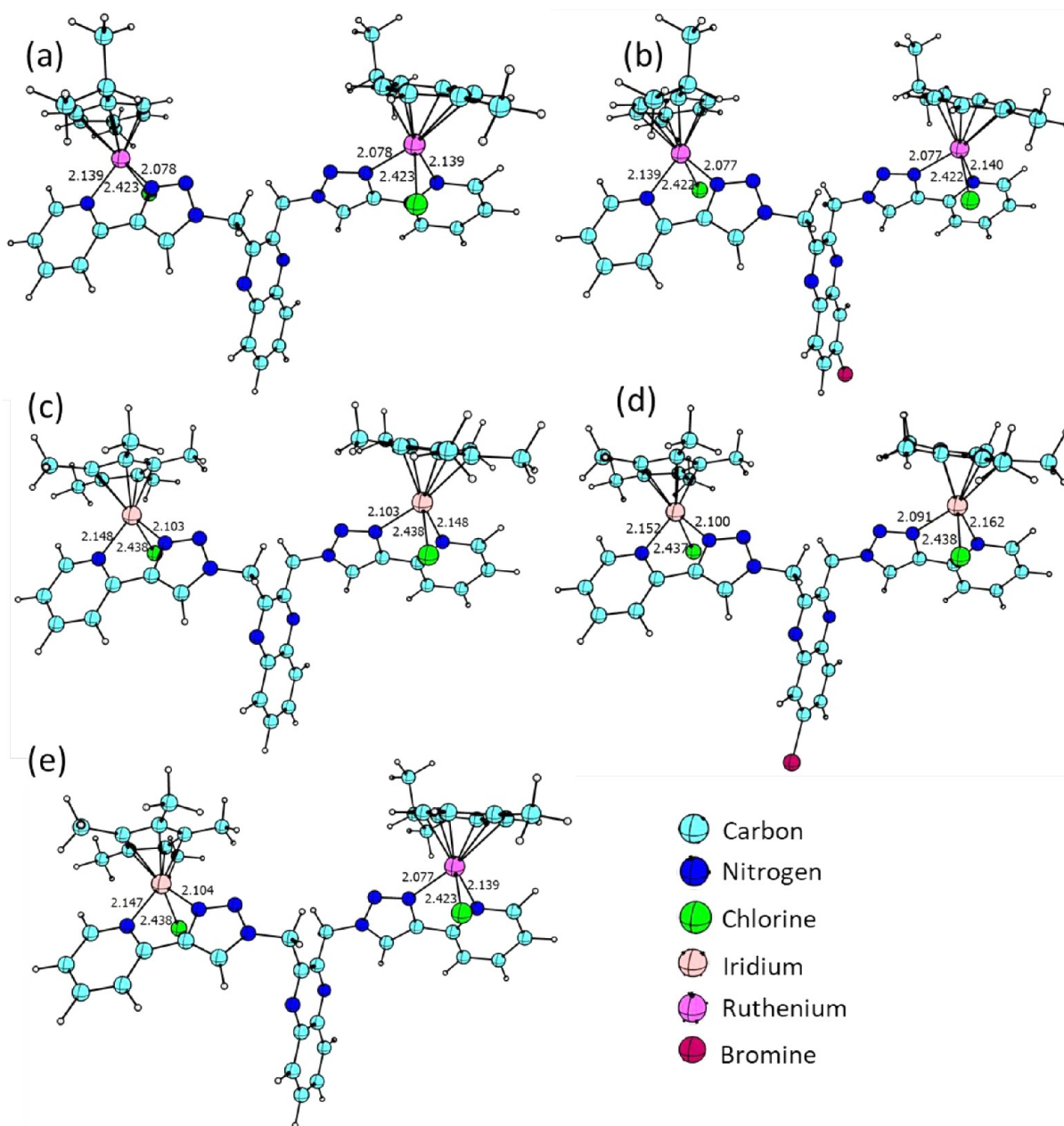


Figure 3. DFT (B3LYP/6-31G**, LANL2DZ) computed structure of the complexes (a) $[\text{Ru}_2\text{L}]$, (b) $[\text{Ru}_2\text{LBr}]$, (c) $[\text{Ir}_2\text{L}]$, (d) $[\text{Ir}_2\text{LBr}]$, and (e) $[\text{RuIrL}]$.

genetic algorithm (LGA) docking parameters.⁶³ The BSA crystal structure (PDB ID: 45FS) is modeled using the Swissmodel online tool, whereas the DNA 3D structure is retrieved from the Protein Data Bank with reference PDB ID 1BNA. The docking complexes were analyzed by using the BIOVia discovery studio.

BSA consists of three major domains (I, II, and III), where the most electrostatic surfaces are found in between the domain-II residues. The complexes were docked randomly with BSA by keeping the coordinates of central grid point of maps to $x = 8.376$, $y = 21.661$, and $z = 106.639$. The best pose of the complexes were located between the domain II and III (Figure 5a). The complexes were bound firmly at the hydrophobic cavity of BSA with the dock score ranging from -3.73 to -6.97 kcal/mol (Table S2). Analyses of the $[\text{Ru}_2\text{L}]$ -BSA docked structure indicated that the best pose is stabilized

by multiple noncovalent interactions of $[\text{Ru}_2\text{L}]$ with the amino acid residues such as ILE297, LEU301, PRO303, LEU304, ARG336, HIS337, and LYS377 (Figure 5c). The higher binding affinity of $[\text{Ru}_2\text{L}]$ complex toward BSA resulted smaller inhibition constant (K_i) of $7.73 \mu\text{M}$. Similarly, other complexes like $[\text{Ir}_2\text{LBr}]$ and $[\text{RuIrL}]$ also showed effective binding at the hydrophobic cavity of BSA with estimated inhibition constants of $23.36 \mu\text{M}$ and $101.51 \mu\text{M}$, respectively.

The docking of metal complexes with DNA were performed by adjusting the coordinates of central grid point of maps to $x = 13.358$, $y = 20.325$, and $z = 10.766$. The metal complexes docking with the DNA dodecamer posed strong electrostatic interactions and a poor hydrophobic cavity. As shown in Figure 4b, the best posed of the complexes $[\text{Ru}_2\text{L}]$, $[\text{Ru}_2\text{LBr}]$, $[\text{Ir}_2\text{LBr}]$, and $[\text{RuIrL}]$ were stacked at one place via interaction by binding to the major groove, whereas the

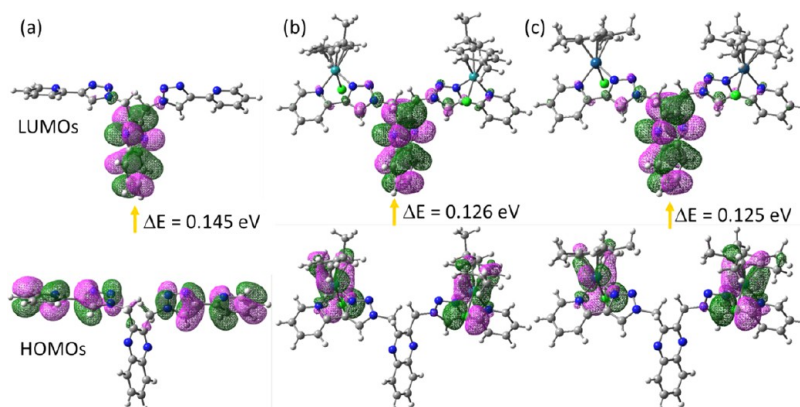


Figure 4. DFT computed electron densities distributions of HOMOs and LUMOs in the ligand L (a) and the complexes $[\text{Ru}_2\text{L}]$ (b) and $[\text{Ir}_2\text{L}]$ (c).

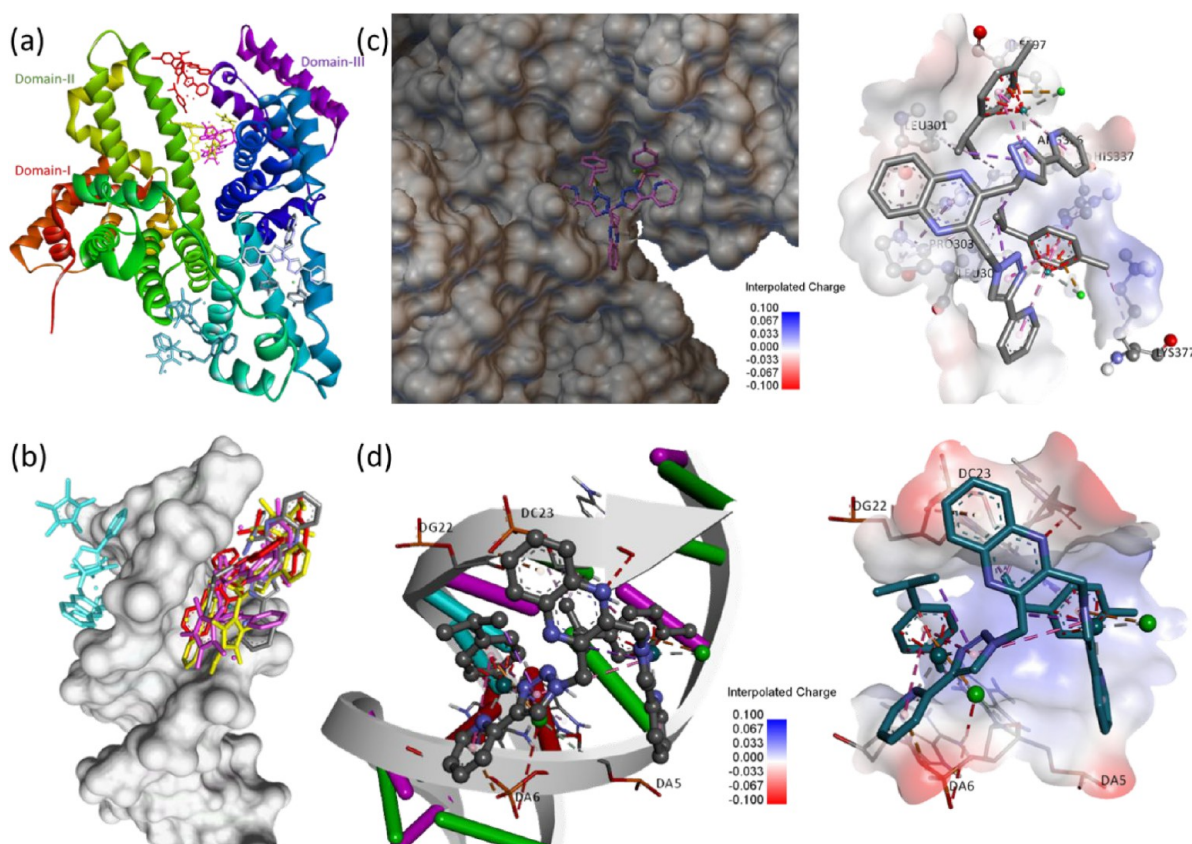


Figure 5. 3D views of the best poses of the $[\text{Ru}_2\text{L}]$, $[\text{Ru}_2\text{LBr}]$, $[\text{Ir}_2\text{L}]$, $[\text{Ir}_2\text{LBr}]$, and $[\text{RuIrL}]$ complexes within the hydrophobic cavity of (a) BSA and (b) DNA. Two views of the docked structures of $[\text{Ru}_2\text{L}]$ with (c) BSA and (d) DNA showing the important interactions with the residues.

complex $[\text{Ir}_2\text{L}]$ bound electrostatically to the outside edge of the minor groove (Figure 5b). The binding energy of the complexes with DNA was observed in the range of -5.53 to -8.21 kcal/mol. Because of the higher affinity of the complexes toward DNA, the inhibition constants are also smaller in comparison to BSA. Complexes like $[\text{Ru}_2\text{L}]$, $[\text{RuIrL}]$, and $[\text{Ir}_2\text{LBr}]$ showed the higher binding affinity with the smaller inhibition constant. With high dock score, the complex $[\text{Ru}_2\text{L}]$ was binding to most favorable sites of DNA base pairs consisting of an electrostatic surface (Figure 5d).

DNA Binding Studies. *UV and Fluorescence Spectroscopic Method.* DNA is the vital pharmacological target for various FDA approved anticancer metallodrugs like cisplatin,

oxaliplatin, and carboplatin and organic drugs (doxorubicin, gemcitabine, 5-fluorouracil, etc.).^{64,53} Therefore, the binding efficacy of metal complexes with DNA is a modern approach for designing effective chemotherapeutic drugs. To investigate experimentally the binding affinity of these complexes with DNA, the reliable electronic absorption titration tool was employed.⁶⁵ There are two different modes of binding of the metal complexes with DNA, i.e., covalent and noncovalent interactions (intercalation, groove binding, and electrostatic interactions).⁶⁵ The UV-vis spectral array of the metal complexes can assuredly unveil the style of interaction of the complexes with DNA. In order to evaluate the equilibrium binding constant (K_b), binding site size (s), and binding mode,

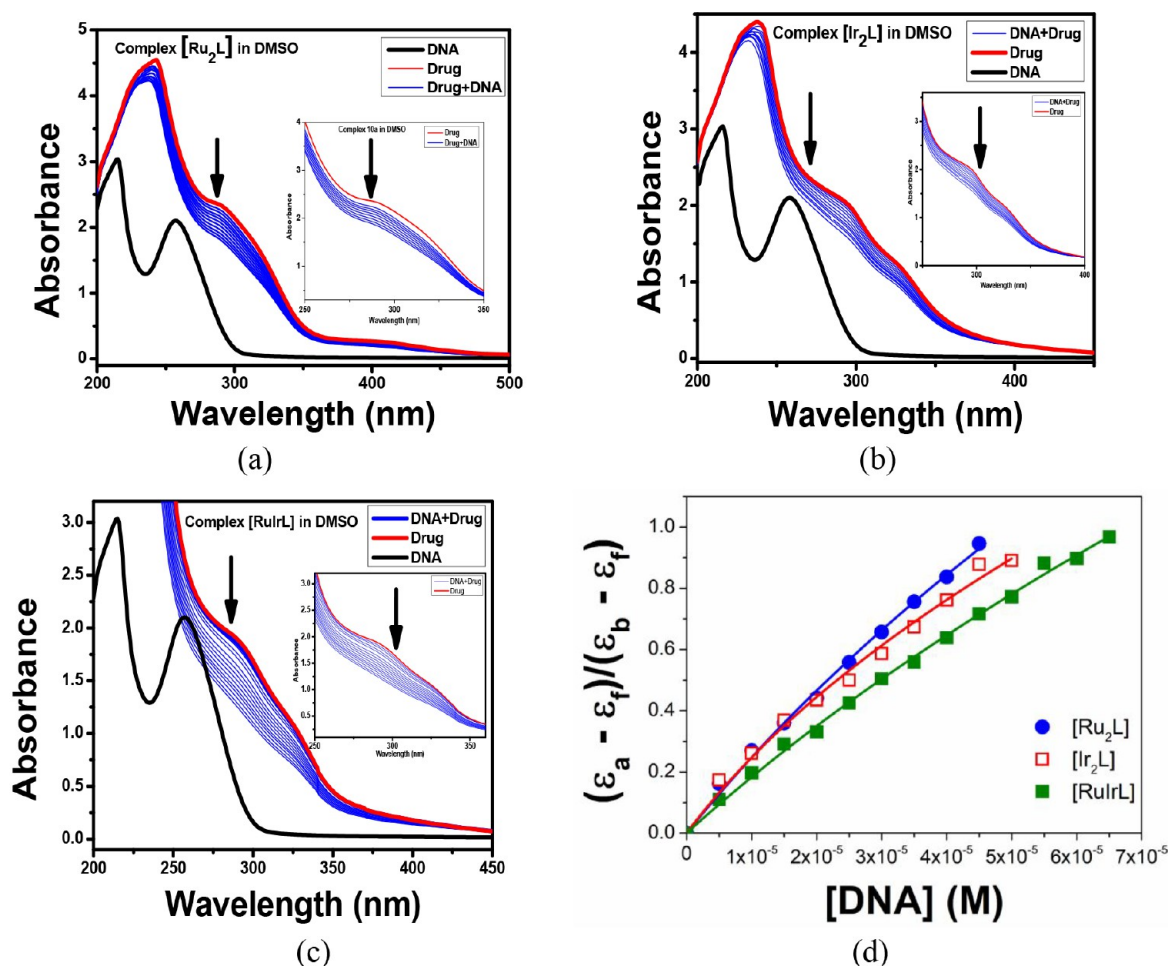


Figure 6. Absorption spectral traces for complexes (a) $[\text{Ru}_2\text{L}]$, (b) $[\text{Ir}_2\text{L}]$, and (c) $[\text{RuIrL}]$ with increasing concentration of ct-DNA in DMSO medium. (d) Plot associated with the titration of $[\text{Ru}_2\text{L}]$, $[\text{Ir}_2\text{L}]$, $[\text{RuIrL}]$, and ct-DNA at 298 K to fit the model of Bard and Thorp.

Table 2. Binding Parameters for Interaction of Complex $[\text{Ru}_2\text{L}]$, $[\text{Ir}_2\text{L}]$, and $[\text{RuIrL}]$ with ct-DNA

complex	K_b (M^{-1}) ^a	S^b	K_{SV} (M^{-1}) ^c	K_{app} (M^{-1}) ^d	hypochromism
$[\text{Ru}_2\text{L}]$	$(0.46 \pm 0.99) \times 10^4$	0.11 ± 0.02	0.0044×10^6	2.7×10^6	26
$[\text{Ir}_2\text{L}]$	$(0.75 \pm 1.30) \times 10^4$	0.21 ± 0.03	0.001×10^6	2.46×10^6	12
$[\text{RuIrL}]$	$(0.44 \pm 0.67) \times 10^4$	0.14 ± 0.06	0.01×10^6	2.8×10^6	43

^a K_b , equilibrium DNA binding constant from UV–visible absorption titration followed by nonlinear curve fitting (MVH model, equation i). ^bBinding site size (per base pair). ^c K_{SV} , Stern–Volmer quenching constant. ^d K_{app} , apparent DNA binding constant from competitive displacement from fluorescence spectroscopy.

the complexes $[\text{Ru}_2\text{L}]$, $[\text{Ir}_2\text{L}]$, and $[\text{RuIrL}]$ (concentration 5×10^{-5} M) were titrated against increasing concentrations of ct-DNA (5 – 60 μM). In all cases, we observed a hypochromism ($\Delta\epsilon \sim 10 \times 10^3$ $\text{M}^{-1} \text{cm}^{-1}$) at $\lambda_{\text{abs}} \sim 300$ nm with respect to an increase in DNA concentration (Figure 6). Bard's equation was employed based on the McGhee–von Hippel (MvH) model to evaluate the equilibrium binding constant (K_b) values and binding site sizes (s , per base pair).^{65g} K_b and s for complexes $[\text{Ru}_2\text{L}]$, $[\text{Ir}_2\text{L}]$, and $[\text{RuIrL}]$ were calculated from equation i, $0.46 \pm 0.99 \times 10^4$ M^{-1} , 0.11 ± 0.02 for $[\text{Ru}_2\text{L}]$; $0.75 \pm 1.30 \times 10^4$ M^{-1} , 0.21 ± 0.03 for $[\text{Ir}_2\text{L}]$; and $0.44 \pm 0.67 \times 10^4$ M^{-1} , 0.14 ± 0.06 for $[\text{RuIrL}]$ in DMSO (Figure 6 and Table 2).

Ethidium Bromide (EtBr) Binding Study. The values of these binding constants are comparable to some reported DNA intercalative Ru(II) complexes (1.1×10^4 – 4.8×10^4

M^{-1})⁶⁶ and lower than the classical DNA intercalator, EtBr (7×10^5 M^{-1}).⁶⁷ Therefore, moderate binding constants with binding site size (s) and significant hypochromism in absorbance on addition of ct-DNA ensured the intercalative mode of binding which had been further justified by an ethidium bromide (EtBr) binding assay.

The competitive binding studies of complexes $[\text{Ru}_2\text{L}]$, $[\text{Ir}_2\text{L}]$, and $[\text{RuIrL}]$ with EtBr–ct-DNA showed a decrease in fluorescence intensity (Figure S8). These complexes displaced EtBr from ct-DNA grooves, and it got bound to the DNA base pairs. Thus, the decrease in fluorescence intensity was observed as EtBr appeared in its free form and thereby free EtBr concentration started to increase gradually in solution. The excitation wavelength used for EtBr-bound DNA and complexes $[\text{Ru}_2\text{L}]$, $[\text{Ir}_2\text{L}]$, and $[\text{RuIrL}]$ was fixed at 485 nm, while the recorded emission wavelength was 600 nm. The

Table 3. Binding Parameters for the Interaction of Complexes [Ru₂L], [Ir₂L], and [RuIrL] with BSA and HSA

complex	K (M ⁻¹) ^a	n_{BSA} ^b	K_{HSA} (M ⁻¹) ^c	K_{q} ^d	K (M ⁻¹) ^e	n_{HSA} ^f
[Ru ₂ L]	0.72×10^4	2.435	0.11×10^6	1.065×10^{13}	0.62×10^4	1.37
[Ir ₂ L]	1.4×10^4	2.508	0.14×10^6	1.38×10^{13}	0.18×10^4	1.71
[RuIrL]	1.33×10^4	2.423	0.05×10^6	0.46×10^{13}	0.75×10^4	1.27

^a K , binding constant with BSA. ^b n_{BSA} , number of binding sites (BSA). ^c K_{HSA} , Stern–Volmer quenching constant. ^d K_{q} , quenching rate constant (HSA). ^e K , binding constant with HSA. ^f n , number of binding sites (HSA).

concentration of DNA and EtBr used was 120 μM and 8 μM respectively. The K_{app} values for the complexes [Ru₂L], [Ir₂L], and [RuIrL] calculated from equation iii were $2.7 \times 10^6 \text{ M}^{-1}$, $2.46 \times 10^6 \text{ M}^{-1}$, and $2.8 \times 10^6 \text{ M}^{-1}$ respectively (Table 2). The value of K_{EtBr} found from literature is $1 \times 10^7 \text{ M}^{-1}$. The Stern–Volmer quenching constant (K_{SV}) calculated from equation iii for the complexes [Ru₂L], [Ir₂L], and [RuIrL] were $0.0044 \times 10^6 \text{ M}^{-1}$, $0.001 \times 10^6 \text{ M}^{-1}$, and $0.01 \times 10^6 \text{ M}^{-1}$ respectively (Table 2). Complex [RuIrL] exhibited highest K_{app} value among all the complexes as the combined property of both Ru(II) and Ir(III) metals were prevailed in heterobinuclear metal complex rather than homobinuclear ruthenium [Ru₂L] and homobinuclear iridium [Ir₂L] complexes.

Viscosity Measurement. In order to find out the binding modes of these complexes with DNA, a hydrodynamic method type viscosity study had been conducted. Binding via intercalation causes the adjacent base pairs separation to yield binding of drug molecules into the DNA double helix, which leads to an increase of the length of DNA as well as their viscosity. In the relative viscosity analysis, a faster increase in the viscosity with the gradual increase in the ratio of drug to ct-DNA in case of complex [RuIrL] was observed, which indicated strong intercalative binding action (Figure S9).

BSA and HSA Binding Study. The fluorescence emission spectra of BSA in the absence and presence of complexes [Ru₂L], [Ir₂L], and [RuIrL] were recorded with excitation at 280 nm while the emission was obtained at 350 nm (Figure S10)^{65e,f}. The concentrations of complexes used for emission spectra were 0–100 μM in distilled water, and the BSA concentration was fixed at 5 μM . The nonlinear and upward curvature of the Stern–Volmer plot suggested that more than one processes were involved in the overall quenching of BSA (Figure S11). The binding affinity (K) of these complexes was calculated from Scatchard plot analysis showing strong binding propensity of the tested complexes with BSA, which was required for transport of protein-bound complexes in biological systems (equation v, Figure S12, Table 3).

In order to find out the applicability of these complexes in the human body, we emphasized the binding study with human serum albumin (HSA) following a similar fluorescence quenching method like BSA (Figure S13). This study revealed the strong binding affinity of the complexes with HSA, which was supported by the Stern–Volmer quenching constant (K_{HSA}), quenching rate constant (K_{q}), and binding constant (K) (equations iv and v, Figure S14, Figure S15, and Table 3). The values of K_{HSA} for all the complexes were observed in the range of 0.05 – $0.14 \times 10^6 \text{ M}^{-1}$. Complex [RuIrL] showed the highest binding constant (K) (0.75×10^4) among the others. On the other hand, the bimolecular quenching rate constant (K_{q}) for these complexes was obtained on the order of 10^{13} . This higher order of quenching rate constant surpassed the maximum value for dynamic quenching ($2 \times 10^{10} \text{ L mol}^{-1} \text{ s}^{-1}$) due to molecular collision, suggesting the successful bimolecular quenching along with complex formation.^{65f} As a

result, the nonlinearity of the Stern–Volmer plot for the complexes with upward curvature can vividly demonstrate the key role of both static and dynamic quenching in the overall fluorescence quenching of HSA.

Biology. Cytotoxic Activity. The *in vitro* cytotoxicity of all these complexes [Ru₂L], [Ru₂LBr], [Ir₂L], [Ir₂LBr], and [RuIrL] was studied using standard 3-(4,5-dimethylthiazol-2-yl)-2,5-diphenyltetrazolium bromide (MTT) assay protocol beside a panel of cancer cell lines, i.e., human epitheloid cervix carcinoma (HeLa) and colorectal adenocarcinoma cells (Caco-2), and one normal cell line, i.e., human embryonic kidney cells (HEK-293) in triplicates. Cisplatin had been used as standard positive control drug. All the complexes exhibited significant cytotoxicity (5–23 μM) in the Caco-2 cell line, but in HeLa cells, compounds [Ir₂L] ($\text{IC}_{50} = 23.4 \pm 0.9 \mu\text{M}$) and [RuIrL] ($\text{IC}_{50} = 14.2 \pm 1.2 \mu\text{M}$) showed considerable potency. Most of the complexes represented higher cytoselectivity than cisplatin against all the human cancer cell lines tested. Among them, complex [RuIrL] displayed the highest potency and selectivity in both the cell lines (HeLa, $\text{IC}_{50} = 14.2 \pm 1.2 \mu\text{M}$, selectivity >14; Caco-2, $\text{IC}_{50} = 2.2 \pm 0.4 \mu\text{M}$, selectivity >90) over the noncancerous HEK-293 cell line (Table 4) as it acquired the

Table 4. Preliminary MTT Cytotoxicity Screening of Synthesized Multinuclear Ru(II) and Ir(III) Complexes at 48 h of Drug Exposure

compound	IC_{50} (μM) ^a			SF ^b	
	Caco-2	HeLa	HEK 293	Caco-2	HeLa
[Ru ₂ L]	5 ± 0.8	50.5 ± 1.1	>200	>40	>4
[Ru ₂ LBr]	12 ± 1.1	>100	>200	>17	2
[Ir ₂ L]	11 ± 1.0	23.4 ± 0.9	>200	>18	>9
[Ir ₂ LBr]	23 ± 2.1	>100	>200	>9	2
[RuL]	17 ± 1.2	65.9 ± 1.0	>200	>12	>3
[IrL]	8 ± 0.8	70.5 ± 0.8	>200	>25	>3
[RuIrL]	2.2 ± 0.4	14.2 ± 1.2	>200	>90	>14
DMSO	–	–	–	–	–
cisplatin	19.8 ± 1.2	14.5 ± 0.9	>50	>2.5	>3.4

^a IC_{50} is the concentration of the synthesized complexes and cisplatin at which 50% of cells undergo cytotoxic cell death under treatment. ^bSF (selectivity factor) = ratio of IC_{50} for HEK-293 to IC_{50} for all the cancer cell lines.

highest lipophilicity, good solubility, and stability in the cancer cell environment along with the synergistic effect of both ruthenium(II) and iridium(III) metals.⁶⁸

The *in vitro* cytotoxicity of the complexes [Ir₂L] and [RuIrL] was further determined by MTT assay with the most aggressive colorectal carcinoma cell line, HT-29. The tumor cells were incubated with the test compounds at different concentrations (1–30 μM for [Ir₂L] and 2.5–20 μM for [RuIrL] for 48 h *in vitro*. It was found that both the complexes exhibited cytotoxicity on the colon cancer cell line (HT29) in a dose dependent manner. Morphologically, cell shrinkage and

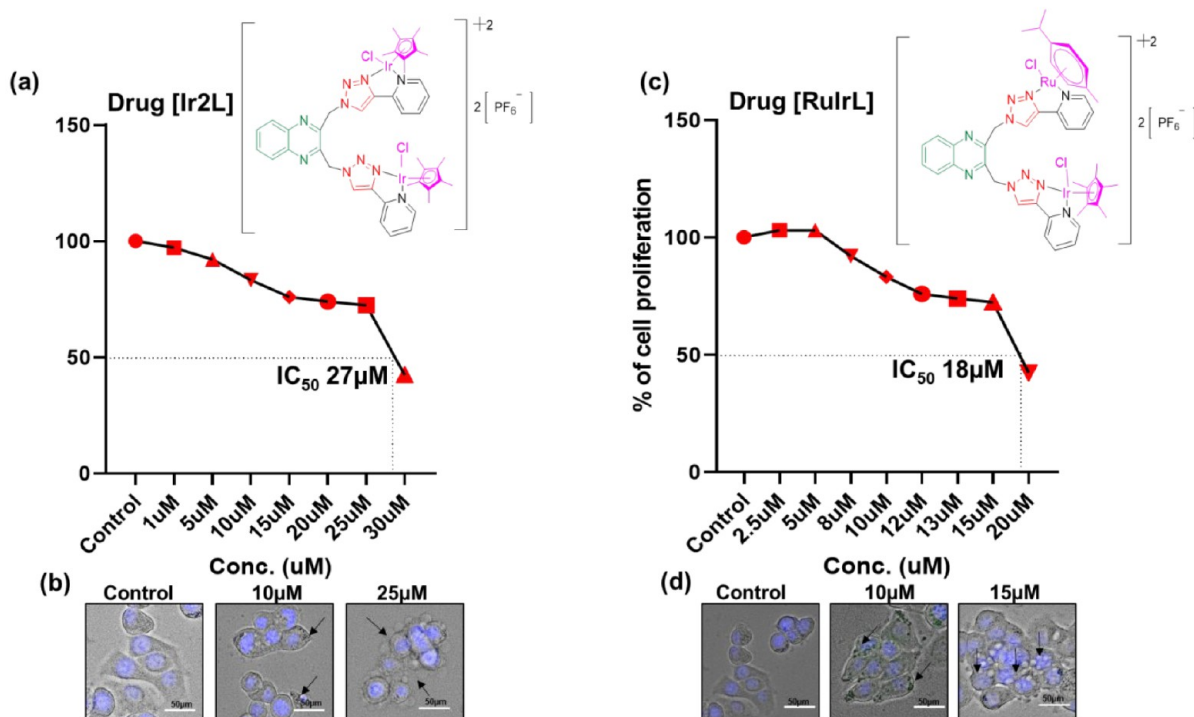


Figure 7. MTT assay and EC_{50} value determination of HT-29 cells upon treatment with (a) $[Ir_2L]$ and (c) $[RuIrL]$ drugs. (b and d) Dose dependent morphological changes of the HT-29 cell line, upon treatment with various doses of drug $[Ir_2L]$ and $[RuIrL]$. Cells were costained with Hoechst 33342 to visualize the nucleus. An arrow mark represents the cell damage. Scale bar $50 \mu m$.

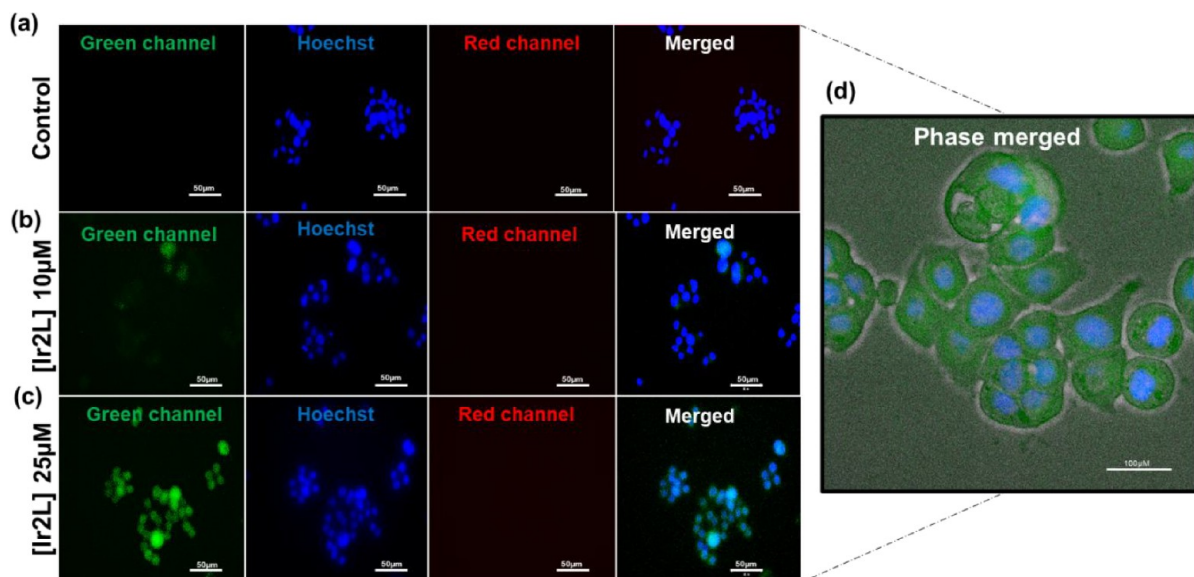


Figure 8. Co-localization of the drug $[Ir_2L]$ in colon cancer cell line HT-29. (a) Control, (b) $10 \mu M$, and (c) $25 \mu M$ of $[Ir_2L]$ treatment for 48 h. (d) Representative image of the drug localization of $[Ir_2L]$ in the highest dose ($25 \mu M$), merged with the phase contrast field. Scale bar $50 \mu m$.

stress granules were observed upon treatment with 10 and $25 \mu M$ of $[Ir_2L]$ and 10 and $15 \mu M$ of $[RuIrL]$ complex (Figure 7). In HT-29 cells, the compound $[Ir_2L]$ showed an EC_{50} value of $27 \mu M$ (Figure 7a) while $[RuIrL]$ showed an EC_{50} value of $18 \mu M$ (Figure 7c). Both complexes were localized in the cytoplasm of the HT-29 cancer cell line upon treatment. Since most of the morphological changes and cellular changes were observed within a 10 – $25 \mu M$ range for $[Ir_2L]$ and a 10 – $15 \mu M$ range for $[RuIrL]$ complex, we chose the aforementioned doses to proceed with further studies.

Morphological Analysis. To explore the action of these complexes on the cancer cell morphology, we treated the cancer cells with the test compounds at two different concentrations ($[Ir_2L]$ at 10 and $25 \mu M$ and $[RuIrL]$ at 10 and $15 \mu M$) along with a control experiment. After 48 h of treatment, costaining was performed with the live cell nuclear stain Hoechst 33342.⁶⁹ Significant cell damage including cell shrinkage and stress granules was observed in the HT-29 cell line (Figure 7, parts b and d), and the changes were compared with the control cell. Cell damage had started to manifest at 10

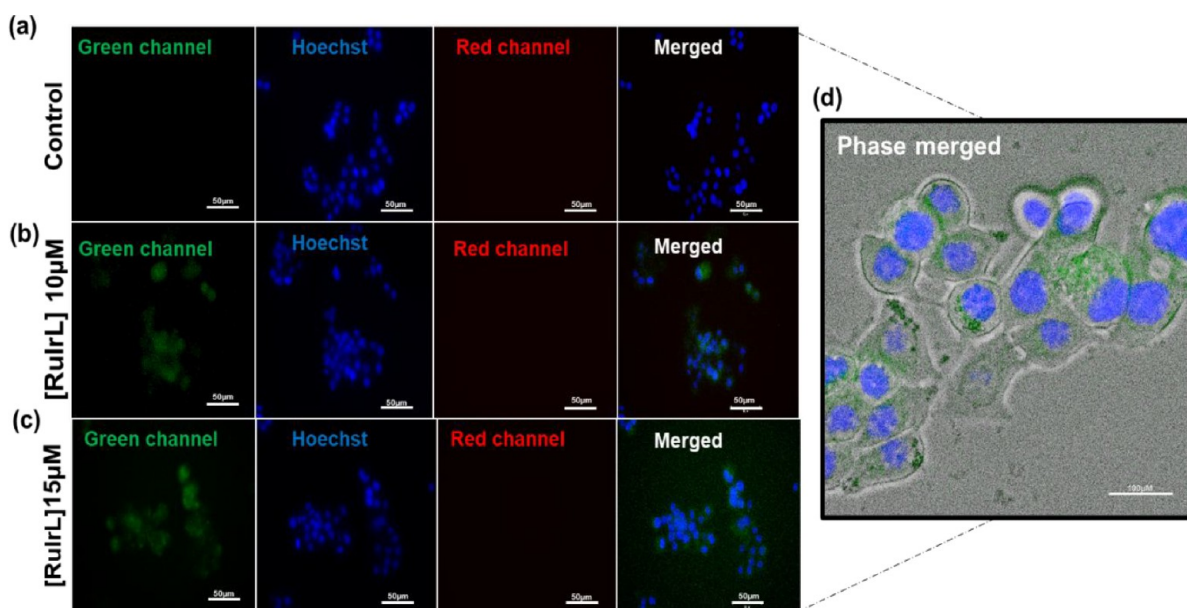


Figure 9. Co-localization of the drug $[\text{RuIrL}]$ in colon cancer cell line HT-29. (a) Control, (b) $10\ \mu\text{M}$, and (c) $15\ \mu\text{M}$ of $[\text{RuIrL}]$ treatment for 48 h. (d) Representative image of the drug localization of $[\text{RuIrL}]$ in the highest dose ($15\ \mu\text{M}$), merged with the phase contrast field. Scale bar $50\ \mu\text{m}$.

μM of $[\text{Ir}_2\text{L}]$ treatment, and the damages were increased with a complex concentration of $25\ \mu\text{M}$ (Figure 7b). On the other hand, complex $[\text{RuIrL}]$ exhibited the effect from 10 to $15\ \mu\text{M}$ (Figure 7d). Maximum cell damages as compared to intact control cells were observed at $25\ \mu\text{M}$ and $15\ \mu\text{M}$ for the complexes $[\text{Ir}_2\text{L}]$ and $[\text{RuIrL}]$ respectively (Figure 7, parts b and d).

Cell Localization Study. To obtain the information on subcellular localization of the complexes $[\text{Ir}_2\text{L}]$ and $[\text{RuIrL}]$, colocalization experiments were performed. As shown in Figure 8, there is a good superposition of green fluorescence emission by the compound $[\text{Ir}_2\text{L}]$ at $25\ \mu\text{M}$ concentration suggesting the penetration of the drug inside the cancer cell membrane and then confirming the subcellular localization of the complex in cytoplasm but not in nucleus. Congruently, the complex $[\text{RuIrL}]$ had also shown a green fluorescence with lesser intensity than that for the complex $[\text{Ir}_2\text{L}]$ in spite of being a potent compound for the HT-29 cell line (Figure 9). Moreover, we had compared the penetration of both the complexes by dint of measuring the mean fluorescence intensity which suggested greater penetration of the complex $[\text{Ir}_2\text{L}]$ in colon cancer cells in comparison to the $[\text{RuIrL}]$ complex (Figure 10). Therefore, this study helped us to presume the subcellular localization of the complexes $[\text{Ir}_2\text{L}]$ and $[\text{RuIrL}]$ in cytoplasmic mitochondria, which were further corroborated by advanced analysis.

Cell-Cycle Analysis. With reference to the results of the MTT assay, where there was an inhibition of cell proliferation, it was further validated by determination of the cellular morphology and localization of the drug to cancer cells. So, we went ahead to investigate the DNA content by flow cytometry. As shown in the Figure 11, the colon cancer cells exhibited high G0/G1 phase ($\sim 50.82\%$) under control conditions, as expected, and the S phase was $\sim 39.77\%$ with $\sim 9.41\%$ G2/M phase (Figure 11d). The treatment of complex $[\text{Ir}_2\text{L}]$ resulted in diminishing of the S phase to ~ 27.58 in $25\ \mu\text{M}$ in HT-29 colorectal carcinoma cells along with significant gradual increment of the G2/M phase (from ~ 9.41 to ~ 31.36).

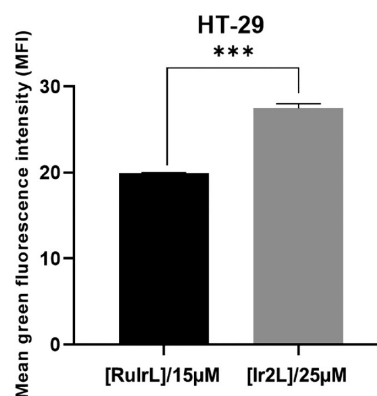


Figure 10. Comparison of the level of penetration of two organometallic complexes $[\text{RuIrL}]$ and $[\text{Ir}_2\text{L}]$ in colon cancer cell line HT-29 cells. Graph represents the mean fluorescence intensity (MFI) of the drugs $[\text{Ir}_2\text{L}]$ and $[\text{RuIrL}]$ at their highest concentrations. The differences between two groups were measured by an unpaired Student *t* test. The *P* values of >0.12 (ns), 0.033 (*), 0.002 (**), and <0.0002 (***) were considered as significant. Error bar represents the \pm standard error of mean (SEM).

Likewise, the complex $[\text{RuIrL}]$, delivered an effect on cell-cycle in the HT-29 colorectal cancer cell line. As illustrated in Figure 12, the colon cancer cells exhibited high G0/G1 phase ($\sim 46.45\%$) under control conditions and high S phase ($\sim 38.30\%$) with $\sim 25.25\%$ G2/M phase (Figure 12d). The treatment of $[\text{RuIrL}]$ resulted in a decrease of the S phase to $\sim 26.38\%$ in $25\ \mu\text{M}$ in HT-29 colorectal carcinoma cells along with a significant increment of the G2/M phase (from ~ 15.26 to $\sim 32.04\%$). In summary, both the organometallic complexes were potent for the colon cancer cell line HT-29 and were able to cause G2/M phase cell cycle arrest. Excessive stalling of the cells at G2/M was a prelude to either cellular damage or apoptosis that demanded further validation (Figure 11 and 12).

Mitotracker RED CMX ROS Staining Assay and Colocalization Assay. Cellular uptake and localization of

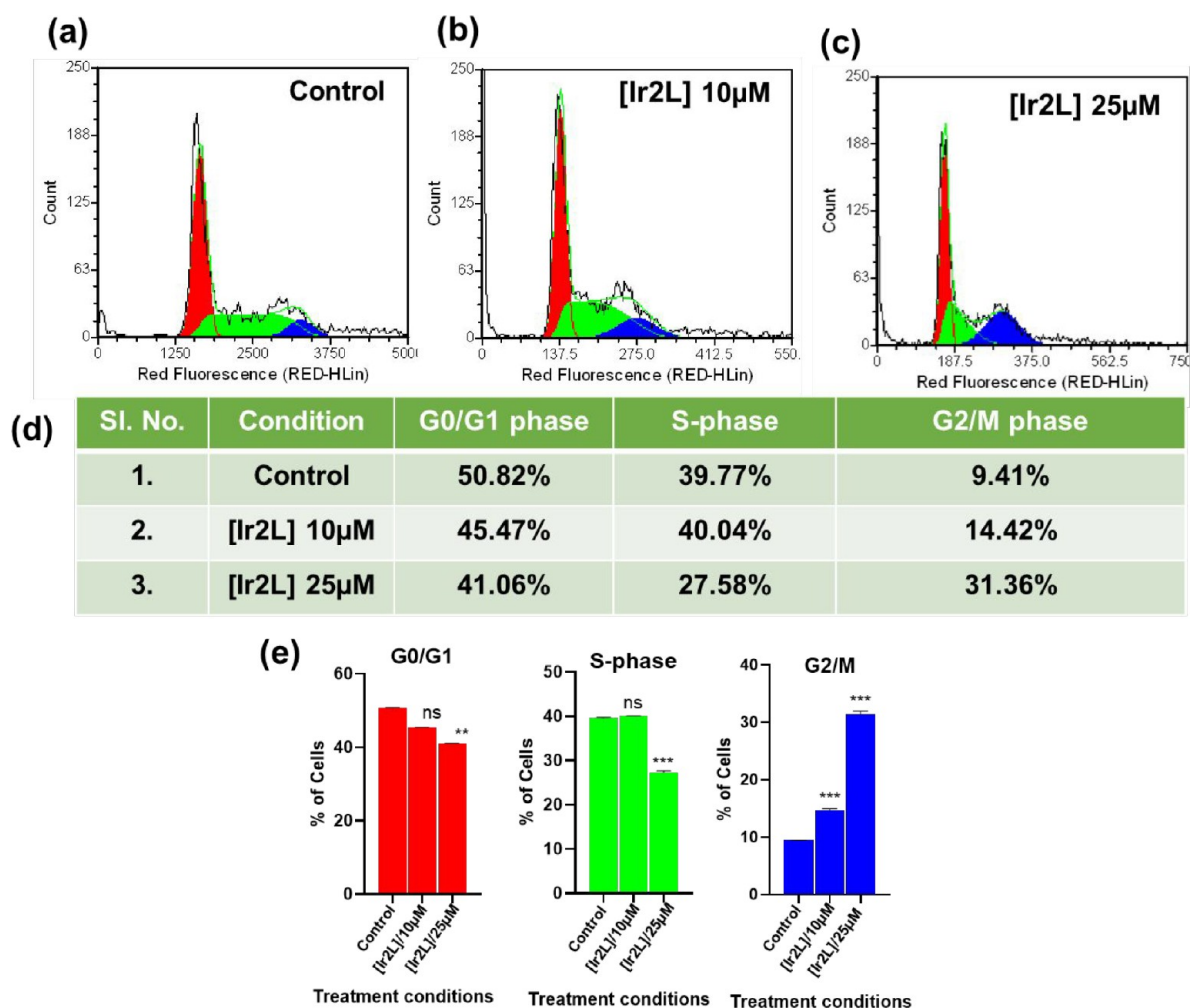


Figure 11. Cell cycle analysis of (a) control HT-29 cells, (b) 10 μM of drug [Ir₂L] treatment, (c) 25 μM of [Ir₂L] drug treatment. (d) Tabular and (e) graphical representation of the different phases of the cell-cycle up on different treatment of the drug [Ir₂L]. The *P* values of >0.12 (ns), 0.033 (*), 0.002 (**), <0.0002 (***) were considered as significant. Error bar represents the \pm standard error of mean (SEM).

an anticancer agent is of major importance to enable it to target key organelles of the cell. As mitochondria plays an important role in detoxifying ROS in the cell, we performed Mitotracker RED CMX ROS staining assay for validating the effect of complexes [Ir₂L] (concentrations 10 and 25 μM) and [RuIrL] (concentrations 10 and 15 μM) on mitochondria along with control experiment. We observed the complex [RuIrL] was being localized in mitochondria causing the mitochondrial damage (Figure 13). The complex [RuIrL] increased the red fluorescence intensity indicated the increasing mass of the mitochondria (Figure 13). Moreover, Mitotracker colocalization assay also revealed the significant mitochondrial localization of these complexes within 48 h of incubation with good Pearson correlation coefficient (0.66–0.67) (Figure 14).

Mitochondrial Dysfunction. Mitochondrial dysfunction acts as a hallmark of cell apoptosis by releasing various proapoptotic proteins. Mitochondrial membrane potential (MMP, $\Delta\Psi\text{m}$) has been recognized as a key indicator of mitochondrial function.³¹ Consequently, JC-1, a MMP-sensitive probe with red fluorescence in normal mitochondria and green fluorescence in dysfunctional mitochondria was used to identify the variation of MMP in HT-29 cells. CCCP (carbonyl cyanide *m*-chlorophenylhydrazone) was used as a

positive control for this type of investigation. In Figures 15a and 16a, it has been shown that the HT-29 cells exposed a uniform red fluorescence without the treatment of complex indicating the normal mitochondrial function. After the treatment of [Ir₂L] and [RuIrL] with HT-29 cells, bright green fluorescence was observed indicating the loss of MMP along with mitochondrial dysfunction which is comparable with the result of CCCP (Figure 15 and 16). Complex [Ir₂L] reduced the mitochondrial membrane potential from 7 to 0.28 (Figure 15b) whereas complex [RuIrL] also decreased the mitochondrial membrane potential to 0.3 (Figure 16b) after 48 h of treatment. Hence, both the potent complexes were capable of affecting mitochondria and thereby their efficiency can be considered as comparable with the positive control CCCP (Figure 15 and 16). In summary, the complexes [RuIrL] and [Ir₂L] were competent to make the mitochondrial membrane “leaky”, leading to damage of mitochondria which resulted in a cell apoptosis pathway.

Structure Activity Relationship Study (SAR). Structure–activity relationship (SAR) study revealed that the potency of pyridinyltriazolylmethylquinoxaline-based Ru(II) and Ir(III) complexes [Ru₂L], [Ir₂L], [Ru₂LBr], [Ir₂LBr], [RuL], [IrL], and [RuIrL] in cancer cells varied with the combination of the metals and substitution of bromine group

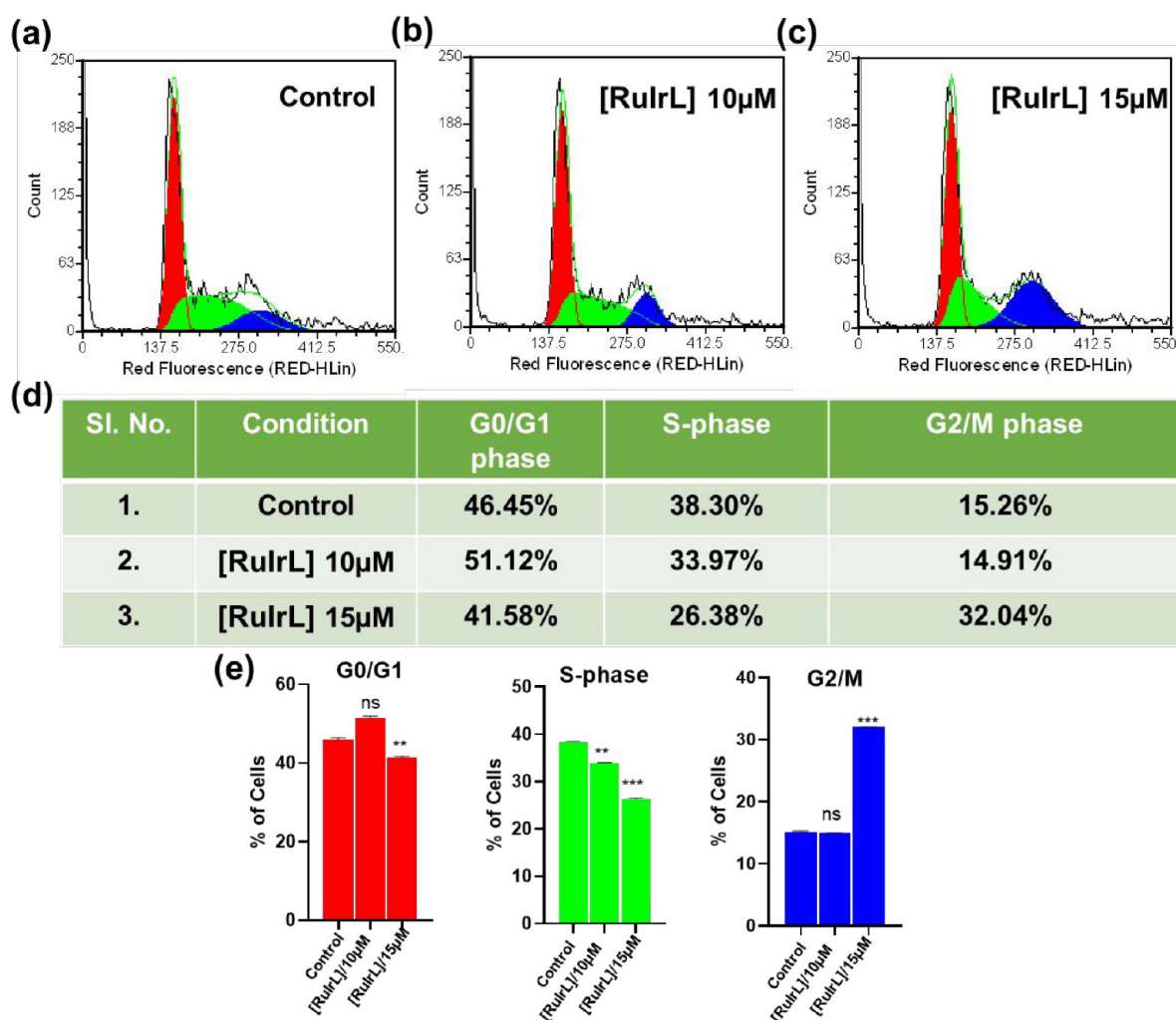


Figure 12. Cell-cycle analysis of (a) control HT-29 cells, (b) 10 μ M of drug [RuIrL] treatment, and (c) 15 μ M of [RuIrL] drug treatment. (d) Tabular and (e) graphical representation of the different phases of the cell-cycle up on different treatment of the drug [RuIrL]. The p values of >0.12 (ns), 0.033 (*), 0.002 (**), and <0.0002 (***) were considered as significant. The error bar represents the \pm standard error of mean (SEM).

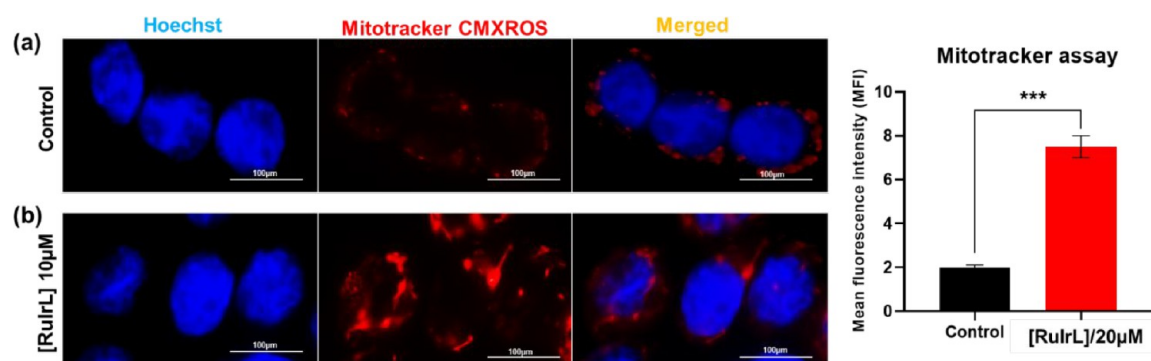


Figure 13. Mitotracker staining assay in HT-29 cell line with the drug [RuIrL] for 48 h (a) untreated control, (b) treated with 10 μ M [RuIrL], (c) graphical representation of the increased MFI in treated colon cancer cells. The differences between the two groups were measured by an unpaired Student t test. The p values of >0.12 (ns), 0.033 (*), 0.002 (**), and <0.0002 (***) were considered as significant. The error bar represents the \pm standard error of mean (SEM). Scale bar 100 μ m.

in the quinoxaline ring. Monoruthenium(II) complex [RuL] showed moderate potency in both the cancer cell lines. However, diruthenium(II) complex [Ru₂L] displayed much better potency in both the cancer cell lines. The dipositive charge of ruthenium triggered the reaction to follow

mitochondrial pathway by reducing the mitochondrial membrane potential (MMP, $\Delta\Psi_m$), but the potency of the complex was reduced significantly after the introduction of a bromo group in the quinoxaline moiety. Similar trends were also observed in case of iridium(III) complexes [IrL], [Ir₂L],

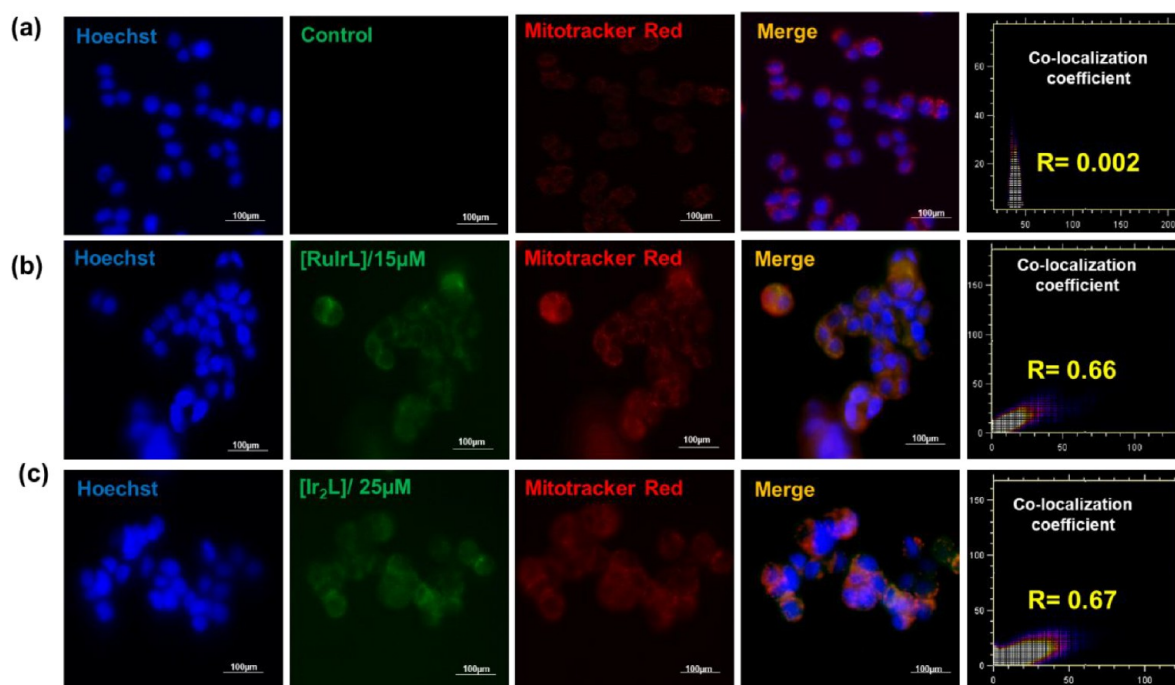


Figure 14. Mitotracker staining assay in HT-29 cell line with the colocalized drug [RuIrL] and [Ir₂L] for 48 h (a) untreated control, (b) treated with 15 μM RuIrL, and (c) treated with 25 μM [Ir₂L] drug. The last image of every panel represents the Pearson correlation coefficient of colocalization. *R*-values between -1 , considered as a strong negative relationship, and $+1$, considered as a strong positive relationship are observed. Scale bar 100 μm .

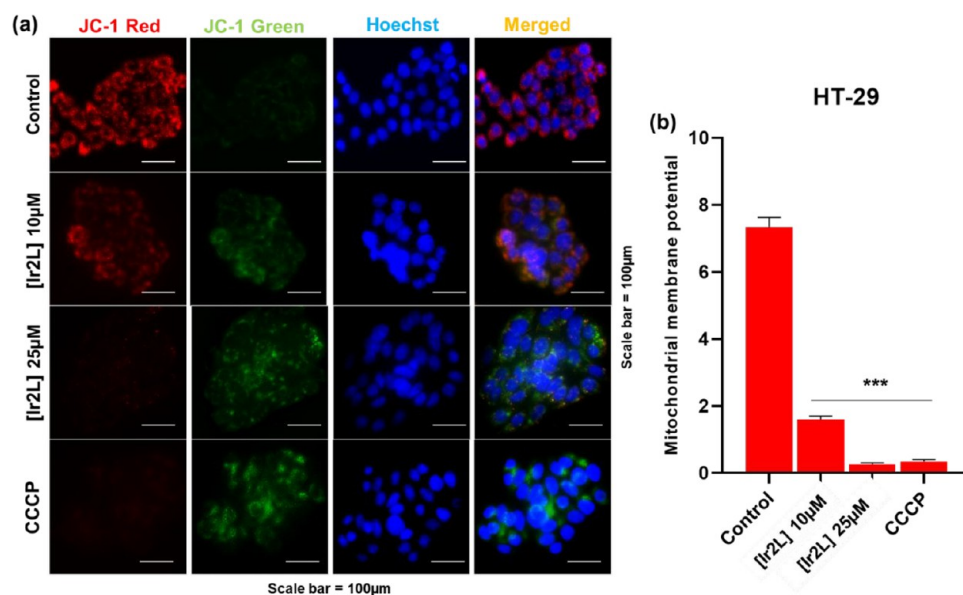


Figure 15. (a) JC-1 staining and the determination of the mitochondrial membrane potential in HT-29 cell line by the drug [Ir₂L]. (b) Graph of JC-1 staining in HT-29 cells upon treatment with drug [Ir₂L] in different concentrations (10 and 25 μM) and positive control CCCP (5 μM). The *P* values of >0.12 (ns), 0.033 (*), 0.002 (**), and <0.0002 (***) were considered as significant. The error bar represents the \pm standard error of mean (SEM). Scale bar 100 μm .

and [Ir₂LBr]. Bis(iridium) complexes [Ir₂L] and [Ir₂LBr] were more potent and selective than bis(ruthenium) complexes [Ru₂L] and [Ru₂LBr] because of their good subcellular (mitochondria) accumulation. The mixed metallic complex [RuIrL] showed highest the cytoselectivity (Caco-2 $>$ 90; HeLa $>$ 14) among all these complexes owing to its high lipophilicity and strong mitochondria targeting ability.

The overall results showed us that (i) hydrophobic *p*-cymene and Cp* ring facilitated the passive diffusion of these

complexes inside the cell, (ii) labile chlorine attached to ruthenium and iridium was essential for several biomolecular interactions, (iii) Ru(II) and Ir(III) bicationic complexes enhanced the compound solubility and accelerated the mitochondrial targeting aptitude by reducing the MMP, (iv) triazolymethylquinoxaline ligand acted as a main protagonist for the DNA intercalating agent, (v) the luminescent property of these complexes helped in the bioimaging application, and (vi) complex [RuIrL] reigned over all the complexes by

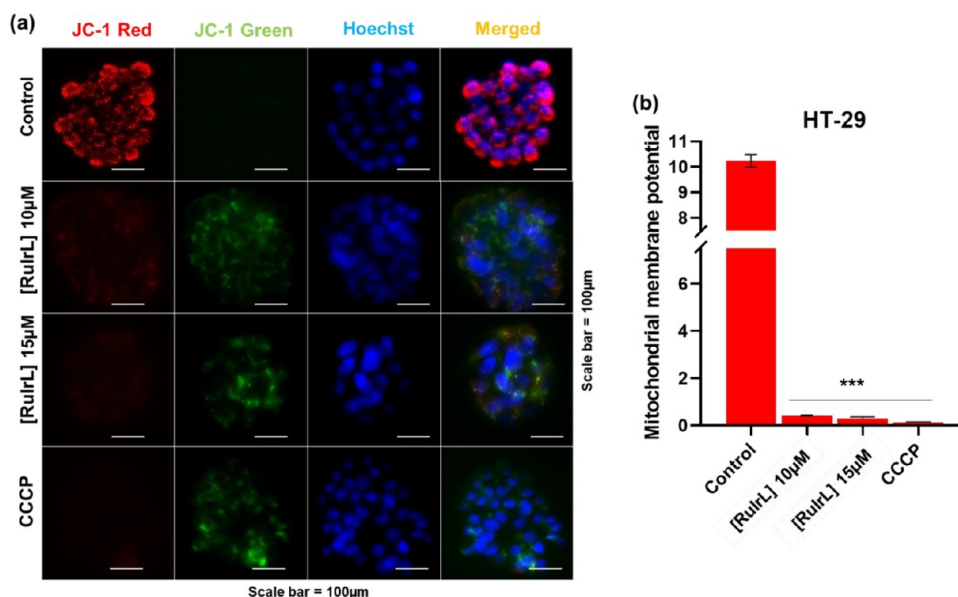


Figure 16. (a) JC-1 staining and the determination of the mitochondrial membrane potential in HT-29 cell line by the drug [RuIrL]. (b) JC-1 staining in HT-29 cells upon treatment with drug LRuIr in different concentrations (10 and 25 μM) and positive control CCCP (5 μM). The P values of >0.12 (ns), 0.033 (*), 0.002 (**), and <0.0002 (***) were considered as significant. The error bar represents the \pm standard error of mean (SEM). Scale bar 100 μm .

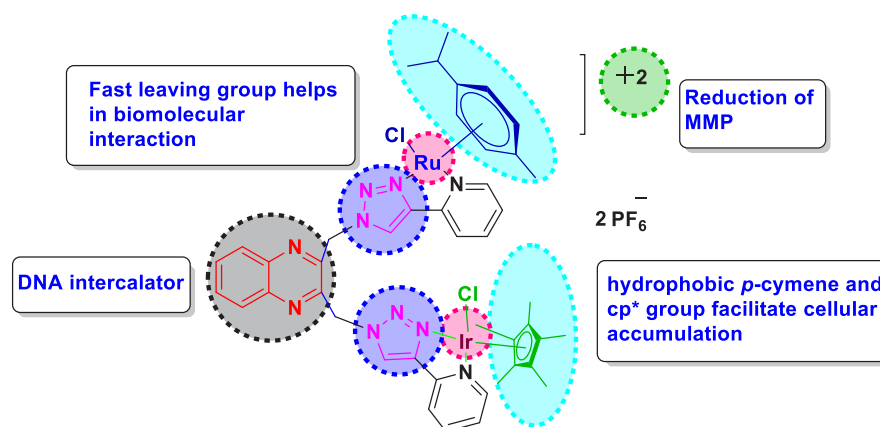


Figure 17. SAR study of pyridinyltriazolymethylquinoxaline-based Ru(II) and Ir(III) complexes [Ru₂L], [Ir₂L], [Ru₂LBr], [Ir₂LBr], [RuL], [IrL], and [RuIrL].

conveying remarkable cytoselectivity because of it attaining the highest lipophilicity, solubility, and stability along with significant subcellular (mitochondria) accumulation reinforced by the synergistic effect of both Ru(II) and Ir(II) metals (Figure 17).

CONCLUSION

From these experiments, it can be nicely portrayed that we have been able to develop mitochondria targeting novel ruthenium- and iridium-based homo and hetero bimetallic pyridinyltriazolymethylquinoxaline complexes as successful luminescent anticancer agents with appreciably high yields and much greater stability to the biological environment. All the prepared complexes displayed their efficiency toward HeLa and Caco-2 cancer cell lines, rendering the normal cell unaffected. However, the heterobimetallic complex [RuIrL] had been able to leave an imprint of its superiority among all of them by exposing its efficiency toward most aggressive colorectal carcinoma cell line, HT-29. The exposition of their

apoptotic power on cancer cells can be demonstrated by their keen targeting affinity toward mitochondria, the power house of the cell triggering mitochondrial dysfunction associated with the reduction of mitochondrial membrane potential making the mitochondrial membrane “leaky” along with the cell cycle arrest. Casting our vision to a DNA binding study also revealed their good DNA intercalative inclination, and their high binding proficiency to human serum albumin (HSA) confirmed their facile transportation to the cellular medium through the bloodstream. In addition to this, the higher quantum yield values attributed the good luminescent nature of the complexes, gifting them an opulent imaging quality. From all the aspects our prepared scaffolds were most active as well as selective in destroying the cancer cells through the detection of cancer cells exploiting their luminescence nature. In a nut shell, it can be depicted that complex [RuIrL] achieved paramount importance over all the complexes on the basis of its excellent potency in association with the highest percent of selectivity to cancer cell along with its superb

cellular imaging quality which will enable it to be explored as an outstanding anticancer theranostic drug in the near future.

EXPERIMENTAL SECTION

Materials and Methods. The highest commercial quality reagents and solvents were used. All analytical grade organic solvents used for the chemical synthesis and chromatography were picked up from E. Merck (India). Sodium ascorbate, copper sulfate, 1,4-dibromo-2,3-butanedione, sodium azide, 2-ethynyl pyridine, *o*-phenylene diamine, $[(\eta^6\text{-}p\text{-cymene})\text{RuCl}(\mu\text{-Cl})_2]$ and $[(\eta^5\text{-Cp}^*)\text{IrCl}(\mu\text{-Cl})_2]$ were purchased from SPECTROCHEM and Sigma-Aldrich Chemical Ltd., Merck. ct-DNA, bovine serum albumin (BSA), and human serum albumin (HSA) were purchased from Sigma-Aldrich Chemical Limited. HeLa, Caco-2, HT-29, and HEK-293 cell lines were purchased from NCCS, Pune, and ATCC. DMEM medium, 1% penicillin and streptomycin, and 1% Glutmax were purchased from Gibco. Also, 10% fetal bovine serum and 0.25% trypsin-EDTA were procured from Himidia and Thermo Fisher Scientific, USA respectively. Hoechst 33342 and carbonyl cyanide *m*-chlorophenylhydrazine (CCCP) were purchased from Sigma-Aldrich Chemical Limited. JC-1 stain was procured from Invitrogen. ^1H NMR, ^{13}C NMR, ^{19}F NMR, and ^{31}P NMR spectra were recorded on a 400 MHz Advance Bruker DPX spectrometer with tetramethylsilane (TMS) as internal standard. The chemical shifts were reported in ppm units. Abbreviations are as follows: s, singlet; d, doublet; dd, double doublet; t, triplet; m, multiplet. The melting points of the complexes were measured on an Elchem Microprocessor based DT apparatus using an open capillary tubes. TLC was performed on silica gel 60 F₂₅₄ precoated aluminum sheets (E. Merck, Germany) using the solvent system hexane, ethyl acetate, and methanol, and solvents and spots were visualized using a UV lamp. Infrared spectra (IR) were recorded on a Shimadzu Affinity FT-IR spectrometer in the range 4000–400 cm^{-1} . The mass spectra of the synthesized compounds were recorded on Applied Biosystems (API-4000 ESI-mode), using methanol as solvent. UV-visible spectra were recorded on a JASCO V-760 spectrometer using a 1 cm quartz cell and fluorescence spectra on a Hitachi F7000 fluorescence spectrophotometer equipped with a xenon lamp. Cyclic voltammetry study was performed by using an electrochemical instrument, FRA2 μ Autolab TypeIII, Potentiostat/galvanostat, Metrohm/Autolab, Netherlands. Conductivity and viscosity were measured using a TDS Conductometer and an Ostwald Viscometer, respectively. For cytotoxicity (MTT assay), Elisa reader and 96-well plate were used. Live cell morphology was observed under an inverted microscope (Primover, Zeiss), and the live cell images were captured using Evos-MS000 fluorescent imager (Invitrogen, Thermo Fisher Scientific).

Synthetic Procedures. Synthesis of 2,3-Bis(bromomethyl)quinoxaline series.⁴⁹ First, 100 mg of *o*-phenylene diamine derivatives were taken in 50 mL beakers followed by addition of 1,4-dibromobutane-2,3-dione (1.1 equiv). The reagents were dissolved in 10 mL of ethanol followed by the addition of silica (100–200 mesh) so as to obtain a slurry. After drying the silica in air, the solid supported reaction mixture was kept in a microwave at 60 W (100 °C) for 10 min. TLC was monitored after every 2 min interval to observe the progress of the reaction using a 3:1 hexane/ethyl acetate solvent system. After the reaction was completed, the solid silica was washed with ethanol (3 times) and filtered off. The obtained filtrate was then evaporated to dryness and recrystallized from hexane/ethyl acetate. Gray crystals of 2, 3-bis(bromomethyl)quinoxaline and 6-bromo-2,3-bis(bromomethyl)quinoxalinewere obtained with 95–98% yield. These compounds were characterized by ^1H and ^{13}C NMR, IR, and mass spectroscopy.

2,3-Bis(bromomethyl)quinoxaline. Yield: 95%. Mp: 150–155 °C. R_f : 0.75 (1:3 ethyl acetate:hexane). ^1H NMR (CDCl_3 , 400 MHz): δ 8.07 (dd, 2H, $J_1 = 6.4$ Hz, $J_2 = 3.6$ Hz, ArH, H-1, H-4), 7.79 (dd, 2H, $J_1 = 6.4$ Hz, $J_2 = 3.6$ Hz, ArH, H-2, H-3), 4.93 (s, 4H, CH_2 , H-9, H-10). ^{13}C NMR (400 MHz, CDCl_3): δ 30.5 (2 \times CH_2 , C-9, C-10), 129.7 (2 \times CH, C-7, C-8), 130.9 (2 \times CH, C-5, C-6), 143.6 (2 \times CH, C-1, C-4), 150.9 (2 \times CH, C-2, C-3). IR (KBr, cm^{-1}): 3018 (sp³ C–

H stretching), 2962 (C–H Ar stretching), 1485 (C–H bending), 1425 (CH_2 bending), 1209(C–N stretching), 765 (C–H stretching of *o*-disubstituted group), 628 (C–Br stretching). ESI-MS (CH_3OH): m/z 317 [$\text{M} + \text{H}$]⁺.

6-Bromo-2,3-bis(bromomethyl)quinoxaline. ^1H NMR (400 MHz, CDCl_3): Yield: 98%. Mp: 165–168 °C. R_f : 0.79 (1:3 ethyl acetate: hexane). ^1H NMR (CDCl_3 , 400 MHz): δ 8.25 (s, 1H, H-4), 7.92 (d, $J = 8.8$ Hz, 1H, H-2), 7.85 (d, $J = 8.8$ Hz, 1H, H-1), 4.89 (s, 4H, CH_2 , H-9, H-10). ^{13}C NMR (400 MHz, CDCl_3): δ 151.8 (CH, C-7), 151.2 (CH, C-8), 142.1 (CH, C-5), 140.3 (CH, C-6), 134.5 (CH, C-4), 131.40 (CH, C-1), 130.3 (CH, C-2), 125.1 (CH, C-3), 30.21 (CH_2 , C-9), 30.11 (CH_2 , C-10). IR (KBr, cm^{-1}): 3028 (sp³ C–H stretching), 2972 (C–H Ar stretching), 1595 (C=C), 1473, 1415 (CH_2 bending), 1209.37 (C–N stretching) 721.38 (C–H stretching of *o*-disubstituted group). 634, 567 (C–Br stretching). ESI-MS (CH_3OH): m/z 395 [$\text{M} + \text{H}$]⁺.

Synthesis of the 2,3-Bis(azidomethyl)quinoxaline Series.⁴⁹ A 50 mg sample of 2,3-bromomethyl quinoxalines and sodium azide was dissolved in ethanol. Then silica was added to the solution and mixed uniformly to obtain a slurry. After complete drying, the reaction mixture was kept in a microwave for 10 min at 40 W (50 °C). TLC was monitored in 3:1 hexane/ethyl acetate solvent system, after every 2 min interval, to observe the change in the reaction. As soon as the reaction was completed, the product from the solid supported mixture was extracted using ethanol. After evaporation of ethanol, blackish crystals of azidomethylquinoxalines were obtained with high yield (~94%).

2,3-Bis(azidomethyl)quinoxaline. Yield: 95%. Mp: 145–148 °C. R_f : 0.68 (1:3 ethyl acetate:hexane). ^1H NMR (CDCl_3 , 400 MHz): δ 8.10 (dd, 2H, $J_1 = 6.4$ Hz, $J_2 = 3.6$ Hz, ArH, H-1, H-4), 7.78 (dd, 2H, $J_1 = 6.4$ Hz, $J_2 = 3.6$ Hz, ArH, H-2, H-3), 4.70 (s, 4H, CH_2 , H-9, H-10). ^{13}C NMR (400 MHz, CDCl_3): δ 148.3 (2 \times CH, C-7, C-8), 140.9 (2 \times CH, C-5, C-6), 130.3 (2 \times CH, C-2, C-3), 128.7 (2 \times CH, C-1, C-4), 52.9 (2 \times CH_2 , C-9, C-10). IR(KBr, cm^{-1}): 3053 (sp³ C–H stretching), 2129, 2083 (N=N=N stretching), 1566 (C–H bending), 1452 (CH_2 bending), 1240 (C–N stretching), 761 (C–H stretching of *o*-disubstituted group). ESI-MS (CH_3OH): m/z 241 [$\text{M} + \text{H}$]⁺.

2,3-Bis(azidomethyl)-6-bromoquinoxaline. Yield: 95%. Mp: 145–148 °C. R_f : 0.68 (1:3 ethyl acetate:hexane). ^1H NMR (CDCl_3 , 400 MHz): δ 8.32 (s, 1H, ArH, H-4), 8.0 (d, 1H, $J = 9.2$ Hz, ArH, H-2), 7.90 (d, 1H, $J = 10.8$ Hz, ArH, H-1), 4.71 (s, 4H, CH_2). ^{13}C NMR (400 MHz, CDCl_3): δ 150.4 (CH, C-7), 149.7 (CH, C-8), 141.9 (CH, C-5), 140.1 (CH, C-6), 134.3 (CH, C-1), 131.5 (CH, C-4), 130.4 (CH, C-2), 124.5 (CH, C-3), 53.3 (CH_2 , C-9), 53.2 (CH_2 , C-10). IR(KBr, cm^{-1}): 3045 (sp³ C–H stretching), 2943 (C–H Ar stretching), 2094, 2069 (N=N=N stretching), 1597 (C–H bending), 1477 (CH_2 bending), 1427 (CH_2 bending), 1143 (C–N stretching), 740 (C–H stretching of *o*-disubstituted group). ESI-MS (CH_3OH): m/z 319 [$\text{M} + \text{H}$]⁺.

Synthesis of the 2,3-Bis[4-(pyridin-2-yl)-1H-1,2,3-triazol-1-yl]methyl]quinoxaline Series (L, LBr).⁴⁹ First, 50 mg of 2,3-bis(azidomethyl) quinoxaline derivatives were taken in 50 mL beakers followed by addition of 2.5 equiv of 2-ethynylpyridine and an aqueous solution of 5 mol % of CuSO_4 and 5 mol % of sodium ascorbate. All the reagents were dissolved properly, and then the required amount of silica was added gradually to make a slurry. After drying in air, the solid supported mixture was kept under microwave at 60 W (100 °C) for 20 min. TLC was monitored every 5 min interval to keep on checking the progression of the reaction. After completion of the reaction, the product was extracted by ethanol washing and then filtered off. The solvent was evaporated to yield a crude triazole product. The fine brown crystals of 2,3-bis[4-(pyridin-2-yl)-1H-1,2,3-triazol-1-yl]methyl]quinoxalines (L, LBr) were obtained from hexane–ethyl acetate (1:1) with a high yield (~95%).

2,3-Bis[4-(pyridin-2-yl)-1H-1,2,3-triazol-1-yl]methyl]quinoxaline (L). Yield: 95%. Mp: 172–177 °C. R_f : 0.26 (ethyl acetate). ^1H NMR (400 MHz, CDCl_3): δ 8.56 (s, 2H, CH, H-19, H-24), 8.38 (s, 2H, CH, H-12, H-14), 8.16 (d, 2H, $J = 6.4$ Hz, CH, H-16, H-21), 8.06–8.09 (m, 2H, CH, H-17, H-22), 7.80–7.83 (m, 2H, CH, H-18, H-23),

7.78 (d, 2H, $J = 8.0$ Hz, CH, H-1, H-4), 7.32 (brs, 2H, CH, H-2, H-3) 6.16 (s, 4H, CH). IR (cm^{-1} , KBr): 3082 (sp^3 C–H stretching), 2970 (C–H Ar stretching), 2833 (CH_2 asymmetric stretching), 1598 (C=C), 1570 (C–H bending), 1450 (CH_2 bending), 1290 (C–N stretching), 783 (CH bending), 756 (C–H stretching of *o*-disubstituted group). ESI-MS (CH_3OH): m/z 447.1 $[\text{M} + \text{H}]^+$.

6-Bromo-2,3-bis[[4-(pyridin-2-yl)-1H-1,2,3-triazol-1-yl]methyl]-quinoxaline (LBr). Yield: 95%. Mp: 295–297 °C. R_f : 0.31 (ethyl acetate). ^1H NMR (400 MHz, $\text{DMSO}-d_6$): δ 8.69–8.73 (m, 2H, CH, H-17, H-23), 8.62 (brs, 2H, CH, H-19, H-24), 8.16 (brs, 1H, CH, H-4), 8.09 (d, $J = 8$ Hz, 2H, CH, H-16, H-21), 7.86–7.94 (m, 3H, CH, H-2, H-18, H-24), 7.37 (brs, 3H, CH, H-1, H-12, H-14), 6.33 (s, 4H, CH₂, H-9, H-10). IR (KBr, cm^{-1}): 3535 (N–H symmetric), 3361 (asymmetric stretching), 2956 (C–H Ar stretching), 1600 (C=C stretching), 1421 (CH_2 bending), 1228 (C–N stretching), 808 (C–H bending), 617 (C–Br stretching). ESI-MS (CH_3OH): m/z 524 $[\text{M} + \text{H}]^+$, 526 $[\text{M} + \text{H}]^+$.

Synthesis of $[(\eta^6\text{-}p\text{-cymene})_2\text{Ru}_2\text{Cl}_2(\text{K}^2\text{-}N,N\text{-}L/\text{LBr})](\text{PF}_6)_2$ ($[\text{Ru}_2\text{L}]$, $[\text{Ru}_2\text{LBr}]$). First, 25 mg (0.0725 mmol) of $[(\eta^6\text{-}p\text{-cymene})\text{RuCl}(\mu\text{-Cl})_2]$ was dissolved in 5 mL of methanol and stirred for 10 min to dissolve the compound completely in methanol. Then 1.1 equiv of previously prepared ligand (**L**, **LBr**) was added to the reaction mixture. The mixture was sonicated for 2 h at ambient temperature. A change in color from deep yellow to deep brown was observed. Then 2.5 equiv of NH_4PF_6 was added to the reaction mixture, which was stirred for another 2 h. The reaction was monitored by TLC using 100% methanol as solvent system. After the completion of the reaction, methanol was evaporated to get the solid product. To remove the impurities, crude product was washed thoroughly with hexane followed by diethyl ether. The purified product was further crystallized from methanol/diethyl ether system, and brown colored fine crystals were obtained with 90–95% yield. The structures of $[\text{Ru}_2\text{L}]$ and $[\text{Ru}_2\text{LBr}]$ were analyzed by ^1H , ^{13}C , ^{19}F , and ^{31}P NMR, FT-IR, and ESI-MS. Purity of these complexes were determined by C, H, N, and HRMS analysis.

$[(\eta^6\text{-}p\text{-cymene})_2\text{Ru}_2\text{Cl}_2(\text{K}^2\text{-}N,N\text{-}L)](\text{PF}_6)_2$ ($[\text{Ru}_2\text{L}]$). Yield: 50.4 mg (0.0394 mmol, 97%). M_r ($\text{C}_{44}\text{H}_{46}\text{N}_{10}\text{Cl}_2\text{F}_{12}\text{P}_2\text{Ru}_2$) = 1277.88 g/mol. Anal. Calcd for $\text{C}_{44}\text{H}_{46}\text{N}_{10}\text{Cl}_2\text{F}_{12}\text{P}_2\text{Ru}_2$: C, 41.36; H, 3.63; N, 10.96. Found: C, 41.05; H, 3.55; N, 10.46. Yield: 97%. Mp: 178–180 °C. R_f (100% methanol): 0.30. ^1H NMR ($\text{DMSO}-d_6$, 400 MHz): δ 9.52 (d, $J = 5.2$ Hz, 2H, H-19, H-24), 9.39 (s, 2H, H-12, H-14), 8.38 (d, $J = 7.6$ Hz, 2H, H-16, H-21), 8.27 (t, $J = 7.6$ Hz, 2H, H-17, H-22), 7.80–7.87 (m, 4H, H-2, H-3, H-18, H-23), 7.73 (t, $J = 6.8$ Hz, 2H, H-1, H-4), 6.62–6.76 (m, 4H, H-9, H-10), 6.14–6.18 (m, 4H, *p*-cymene H-3a, H-4a, H-5a, H-6a), 6.03 (d, $J = 6.0$ Hz, 2H, *p*-cymene H-3b, H-4b), 5.87 (d, $J = 5.6$ Hz, 2H, *p*-cymene H-5b, H-6b), 2.62–2.69 (m, 2H, CH, H-8a, H-8b), 2.18 (s, 6H, Me, H-1a, H-1b), 1.08 (d, $J = 6.8$ Hz, 6H, *p*-cymene, H-9a, H-9b), 1.01 (d, $J = 6.8$ Hz, 6H, *p*-cymene, H-10a, H-10b). ^{13}C (DMSO- d_6 , 100 MHz): δ 156.3 (C, C-15), 154.0 (C, C-20), 148.4 (2C, C-7, C-8), 146.6 (2CH, C-19, C-24), 140.6 (2C, C-5, C-6), 138.5 (2C, C-11, C-13), 131.6 (2CH, C-17, C-22), 128.9 (CH, C-12), 127.90 (CH, C-14), 126.6 (CH, C-2), 125.9 (CH, C-3), 123.1 (CH, C-1), 122.2 (CH, C-4), 112.1 (2CH, C-16, C-21), 107.0 (2CH, C-18, C-23), 104.2 (*p*-cymene, C, C-2a, C-2b), 103.1 (*p*-cymene, C, C-7a, C-7b), {86.1, 85.6, 83.9, 82.9} (*p*-cymene, 8CH, C-3a, 3b, 4a, 4b, 5a, 5b, 6a, 6b), 54.2 (CH_2 , C-9, C-10), 30.9 (*p*-cymene, CH, C-8a, C-8b), {22.3, 21.9} (*p*-cymene, isopropyl CH_3 , C-9a, C-10a, C-9b, C-10b), 18.7 (*p*-cymene, CH_3 , C-1a, C-1b). ^{19}F NMR ($\text{DMSO}-d_6$, 376 MHz): δ -71.01 (PF_6), -69.12 (PF_6). ^{31}P NMR ($\text{DMSO}-d_6$, 162 MHz): δ -153.04 (PF_6), -148.65 (PF_6), -144.26 (PF_6), -139.87 (PF_6), -135.47 (PF_6). IR (cm^{-1} , KBr): 3122 (C–H stretching), 2970 (sp^3 C–H stretching), 1622 (C=C), 1442 (C=C stretching), 1280 (C–N stretching), 829 (P–F stretching), 773 (C–H bending). ESI-MS (MeOH): m/z 493.9 $[\text{M} - 2\text{PF}_6]^{2+}$. HRMS (MeOH): $\text{C}_{44}\text{H}_{46}\text{N}_{10}\text{Cl}_2\text{F}_{12}\text{P}_2\text{Ru}_2$ (M) calculated m/z , 494.0686 $[\text{M} - 2\text{PF}_6]^{2+}$, 1301.0552 $[\text{M} + \text{Na}]^+$; observed m/z , 494.0699 $[\text{M} - 2\text{PF}_6]^{2+}$, 1301.0549 $[\text{M} + \text{Na}]^+$.

$[(\eta^6\text{-}p\text{-cymene})_2\text{Ru}_2\text{Cl}_2(\text{K}^2\text{-}N,N\text{-}L\text{Br})](\text{PF}_6)_2$ ($[\text{Ru}_2\text{LBr}]$). Yield: 52.5 mg (0.0386 mmol, 95%). M_r ($\text{C}_{44}\text{H}_{45}\text{N}_{10}\text{BrCl}_2\text{F}_{12}\text{P}_2\text{Ru}_2$) = 1356.77 g/mol. Anal. Calcd for $\text{C}_{44}\text{H}_{45}\text{N}_{10}\text{BrCl}_2\text{F}_{12}\text{P}_2\text{Ru}_2$: C, 38.95; H, 3.34;

N, 10.32. Found: C, 38.46; H, 3.39; N, 10.02. Yield: 95%. Mp: 185–187 °C. R_f (100% methanol): 0.34. ^1H NMR ($\text{DMSO}-d_6$, 400 MHz): δ 9.49 (brs, 2H, H-19, H-24), 9.35 (brs, 2H, H-12, H-14), 8.33 (s, 2H, H-16, H-21), 8.25 (s, 2H, H-17, H-22), 7.97 (brs, 2H, H-1, H-4), 7.72 (brs, 3H, H-2, H-18, H-23), 6.66 (brs, 4H, H-9, H-10), 5.97–6.00 (m, $J = 5.60$ Hz, 3H, *p*-cymene, H-3a, H-3b, H-4a), 5.83 (d, 2H, $J = 6.0$ Hz, *p*-cymene, H-5a, H-6a), 5.78 (d, $J = 6.0$ Hz, 2H, *p*-cymene, H-4b, H-5b), 5.74 (d, $J = 6.0$ Hz, 1H, *p*-cymene, H-6b), 2.74–2.85 (sept, 2H, *p*-cymene, H-8a, H-8b), 2.17 (s, 3H, *p*-cymene, H-1a), 2.16 (s, 3H, *p*-cymene, H-1b), 1.08 (d, $J = 6.8$ Hz, 6H, *p*-cymene, H-9a, H-9b), 1.0 (d, $J = 6.0$ Hz, H-10a, H-10b). ^{13}C (DMSO- d_6 , 100 MHz): δ {156.9, 156.3} (2C, C-15, C-20), 149.5 (2C, C-7, C-8), 148.4 (CH, C-19), 146.7 (CH, C-24), 141.4 (C, C-5), 140.7 (C, C-6), 139.4 (2CH, C-17, C-22), 134.7 (CH, C-4), 131.4 (2C, C-11, C-13), 130.7 (2CH, C-12, C-14), 128.1 (CH, C-1), 126.5 (CH, C-2), 124.4 (CH, C-16, C-21), 123.1 (CH, C-18, C-23), 106.8 (C, C-3), 104.1 (*p*-cymene, C, C-2a, C-2b), 100.6 (*p*-cymene, C, C-8a, C-8b), {86.8, 85.9, 85.6, 84.8} (*p*-cymene, Ar–CH, C-3a, 3b, 4a, 4b, 5a, 5b, 6a, 6b), 54.1 (CH_2 , C-9, C-10), {30.9, 30.4} (*p*-cymene, isopropyl-CH, C-8a, C-8b), {22.4, 22.3, 21.9, 21.8} (*p*-cymene, isopropyl CH_3 , C-9a, C-9b, C-10a, C-10b), {18.7, 18.3} (*p*-cymene, CH_3 , C-1a, C-1b). ^{19}F NMR ($\text{DMSO}-d_6$, 376 MHz): δ -71.02 (PF_6), -69.13 (PF_6). ^{31}P NMR ($\text{DMSO}-d_6$, 162 MHz): δ -157.42 (PF_6), -153.03 (PF_6), -148.64 (PF_6), -144.25 (PF_6), -139.86 (PF_6), -135.47 (PF_6), -131.08 (PF_6). IR (cm^{-1} , KBr): 3622 (C–H stretching), 2966 (Sp^3 C–H stretching), 1624 (N–H bending), 1440 (arm C=C stretching), 1278 (C–N stretching), 827 (P–F stretching). ESI-MS (MeOH): m/z : 533.0 $[\text{M} - 2\text{PF}_6]^{2+}$. HRMS (MeOH): m/z 533.4242. HRMS (MeOH): $\text{C}_{44}\text{H}_{45}\text{N}_{10}\text{BrCl}_2\text{F}_{12}\text{P}_2\text{Ru}_2$ (M) calculated m/z , 535.0233 $[\text{M} - 2\text{PF}_6]^{2+}$, 1380.9657 $[\text{M} + \text{Na}]^+$; observed m/z , 535.0247 $[\text{M} - 2\text{PF}_6]^{2+}$, 1380.9643 $[\text{M} + \text{Na}]^+$.

Synthesis of $[(\eta^5\text{-}Cp^*)_2\text{Ir}_2\text{Cl}_2(\text{K}^2\text{-}N,N\text{-}L/\text{LBr})](\text{PF}_6)_2$ ($[\text{Ir}_2\text{L}]$, $[\text{Ir}_2\text{LBr}]$). First 25 mg (0.017 mmol) of $[(\eta^5\text{-}Cp^*)\text{IrCl}(\mu\text{-Cl})_2]$ was dissolved in 5 mL of methanol and stirred for 10 min to dissolve the compound completely in methanol. Then 1.1 equiv of the previously prepared ligand (**L**/**LBr**) was added to the reaction mixture. The mixture was sonicated for 2 h at ambient temperature. A change in color from orange to light yellow was observed. Then 2.5 equiv of NH_4PF_6 was added to the reaction mixture, which was stirred for another 2 h. The reaction was monitored by TLC using 100% methanol as solvent system. After the completion of the reaction, methanol was evaporated to obtain the solid product. To remove the impurities, crude product was washed thoroughly with hexane followed by diethyl ether. The purified product was further crystallized from methanol–diethyl ether mixture to get yellow colored fine crystals with 90–95% yield. The structures of $[\text{Ir}_2\text{L}]$ and $[\text{Ir}_2\text{LBr}]$ were analyzed by ^1H , ^{13}C , ^{19}F , and ^{31}P NMR, FT-IR, and ESI-MS. Purity of the complex was determined by C, H, N, and HRMS analysis.

$[(\eta^5\text{-}Cp^*)_2\text{Ir}_2\text{Cl}_2(\text{K}^2\text{-}N,N\text{-}L)](\text{PF}_6)_2$ ($[\text{Ir}_2\text{L}]$). Yield: 45 mg (0.031 mmol, 98%). M_r ($\text{C}_{44}\text{H}_{48}\text{N}_{10}\text{Cl}_2\text{F}_{12}\text{P}_2\text{Ir}_2$) = 1462.19 g/mol. Anal. Calcd for $\text{C}_{44}\text{H}_{48}\text{N}_{10}\text{Cl}_2\text{F}_{12}\text{P}_2\text{Ir}_2$: C, 36.14; H, 3.31; N, 9.58. Found: C, 36.73; H, 3.67; N, 9.73. Yield: 98%. Mp: 178–180 °C. R_f (100% methanol): 0.30. ^1H NMR ($\text{DMSO}-d_6$, 400 MHz): δ 9.45 (s, 2H, H-12, H-14), 8.99 (d, $J = 5.6$ Hz, 2H, H-19, H-24), 8.54 (s, 2H, H-16, H-21), 8.31 (d, $J = 4.8$ Hz, 2H, H-17, H-22), 7.82 (s, 4H, H-2, H-3, H-18, H-23), 7.78 (t, $J = 6.4$ Hz, 2H, H-1, H-4), 6.69 (s, 4H, H-9, H-10), 1.73 (s, 30H, Cp*, H-6a, H-6b, H-7a, H-7b, H-8a, H-8b, H-9a, H-9b, H-10a, H-10b). ^{13}C NMR ($\text{DMSO}-d_6$, 100 MHz): δ 157.2 (C, C-15), 156.5 (C, C-20), 152.9 (2C, C-7, C-8), 149.5 (2CH, C-19, C-24), 148.4 (2C, C-5, C-6), 147.9 (2CH, C-17, C-22), 141.2 (2C, C-11, C-13), 140.9 (CH, C-12), 140.6 (CH, C-14), 131.2 (CH, C-2, C-3), 129.1 (2CH, C-1, C-4), 128.9 (CH, C-16), 127.9 (CH, C-21), 122.9 (2CH, C-18, C-23), {91.8, 91.3, 89.8, 89.4} (Cp*, 10C, C-1a, 1b, 2a, 2b, 3a, 3b, 4a, 4b, 5a, 5b), 54.2 (CH_2 , C-9, C-10), (8.8, Cp*, CH₃, C-6a, 6b, 7a, 7b, 8a, 8b, 9a, 9b, 10a, 10b). ^{19}F NMR ($\text{DMSO}-d_6$, 400 MHz): δ -71.06 (PF_6), -69.17 (PF_6). ^{31}P NMR ($\text{DMSO}-d_6$, 400 MHz): δ -152.98 (PF_6), -153.00 (PF_6), -148.61 (PF_6), -144.22 (PF_6), -139.83 (PF_6), -135.44 (PF_6). IR (cm^{-1} , KBr): 3319 (arm C–H stretching), 3037 (Sp^3 C–H stretching), 1423 (arm C=C stretching), 1282 (C–N stretching), 1124 (C–O stretching), 827

(P–F stretching), 779 (C–H bending). ESI-MS (MeOH): m/z : 586.2 [M – 2PF₆]²⁺. HRMS (MeOH): C₄₄H₄₈N₁₀Cl₂F₁₂P₂Ir₂ (M) calculated m/z , 586.1349 [M – 2PF₆]²⁺, 1485.1880 [M + Na]⁺; observed m/z , 586.1329 [M – 2PF₆]²⁺, 1485.1843 [M + Na]⁺.

[(η⁵-Cp*)₂Ir^{III}Cl₂(K²-N,N-LBr)](PF₆)₂ ([Ir₂LBr]). Yield: 46.0 mg (0.0298 mmol, 95%). *M_r* (C₄₄H₄₇N₁₀BrCl₂F₁₂P₂Ir₂) = 1541.08 g/mol. Anal. Calcd for C₄₄H₄₇N₁₀BrCl₂F₁₂P₂Ir₂: C, 34.29; H, 3.07; N, 9.09. Found: C, 33.80; H, 3.25; N, 8.34. Yield: 95%. Mp: 175–177°C. *R_f* (100% methanol): 0.46. ¹H NMR (DMSO-*d*₆, 400 MHz): δ 9.44 (s, 2H, H-12, H-14), 8.99 (d, *J* = 5.2 Hz, 2H, H-19, H-24), 8.56 (s, 2H, H-16, H-21), 8.33 (t, *J* = 7.2 Hz, 2H, H-17, H-22), 8.05 (s, 1H, H-4), 7.96 (d, *J* = 8.4 Hz, 1H, H-2), 7.76–7.79 (m, 3H, H-1, H-18, H-23), 6.70 (d, *J* = 9.2 Hz, 4H, H-9, H-10), 1.74 (s, 15H, Cp*, H-6a, H-7a, H-8a, H-9a, H-10a). 1.73 (s, 15H, Cp*, H-6b, H-7b, H-8b, H-9b, H-10b). ¹³C NMR (DMSO-*d*₆, 400 MHz): δ 152.9 (2C, C-15, C-20), 148.4 (C, C-7), 147.8 (C, C-8), 145.1 (CH, C-19), 144.5 (CH, C-24), 141.2 (2C, C-5, C-6), 139.4 (2CH, C-17, C-22), 135.7 (C, C-11), 134.5 (C, C-13), 132.8 (CH, C-4), 131.0 (CH, C-21), 128.7 (CH, C-2), 127.9 (CH, C-12), 123.1 (CH, C-14), 120.9 (CH, C-16), 120.2 (CH, C-21), 117.2 (CH, C-18), 112.5 (CH, C-23), 107.4 (C, C-3), {92.6, 91.3, 89.8, 89.4} (Cp*, C, C-1a, 1b, 2a, 2b, 3a, 3b, 4a, 4b, 5a, 5b), 54.2 (CH₂, C-9, C-10), {9.0, 8.9, 8.8, 8.7, 8.1} (Cp*, CH₃, C-6a, 6b, 7a, 7b, 8a, 8b, 9a, 9b, 10a, 10b). ¹⁹F NMR (DMSO-*d*₆, 376 MHz): δ –71.05 (PF₆), –69.16 (PF₆). ³¹P NMR (DMSO-*d*₆, 162 MHz): δ –157.38 (PF₆), –152.99 (PF₆), –148.60 (PF₆), –144.21 (PF₆), –139.82 (PF₆), –135.43 (PF₆). IR (cm^{–1}, KBr): 3327 (arm C–H stretching), 1427 (arm C=C stretching), 1222 (C–N stretching), 825 (P–F stretching), 777 (C–H bending). ESI-MS (MeOH): m/z : 626.8 [M – 2PF₆]²⁺. HRMS (MeOH): C₄₄H₄₇N₁₀BrCl₂F₁₂P₂Ir₂ (M) calculated m/z , 625.0902 [M – 2PF₆]²⁺, 1563.0985 [M + Na]⁺; observed m/z , 625.0899 [M – 2PF₆]²⁺, 1563.0984 [M + Na]⁺.

Synthesis of [(η⁶-*p*-cymene)Ru^{II}Cl(K²-N,N-L)]PF₆ ([RuL]). A 25 mg (0.041 mmol, 0.5 equiv) sample of [(η⁶-*p*-cymene)RuCl(μ-Cl)]₂ was dissolved in 5 mL of methanol and stirred for 10 min to dissolve the compound completely in methanol. Then 38.2 mg (1.1 equiv) of previously prepared ligand (L) was added to the reaction mixture. The mixture was sonicated for 2 h at ambient temperature. As soon as a change in color from deep yellow to deep brown was observed, 1.1 equiv of NH₄PF₆ was added to the reaction mixture which was stirred for another 2 h. The reaction was monitored by TLC using 100% methanol as solvent system. After the complete conversion, methanol was evaporated in order to have the solid product. Then solid crude product was washed thoroughly with 5 mL of hexane and dried to expel the impurities. The purified product was crystallized from methanol–diethyl ether mixture and pure brown colored fine crystals were obtained with 90–95% yield. The structure of [RuL] was examined by ¹H, ¹⁹F, and ³¹P NMR, FT-IR, and ESI-MS. Purity of the sample was determined by HRMS analysis.

[(η⁶-*p*-cymene)Ru^{II}Cl(K²-N,N-L)]PF₆ ([RuL]). Yield: 67 mg (0.078 mmol, 95%). *M_r* (C₃₄H₃₂N₁₀ClF₆PRu) = 862.17 g/mol. Anal. Calcd for C₃₄H₃₂N₁₀ClF₆PRu: C, 47.36; H, 3.74; N, 16.25. Found: C, 47.78; H, 3.32; N, 16.34. Yield: 97%. Mp: 174–176°C. *R_f* (100% methanol): 0.36. ¹H NMR (DMSO-*d*₆, 400 MHz): δ 9.53 (d, *J* = 5.2 Hz, 1H, H-19), 9.42 (s, 1H, H-24), 8.75 (s, 1H, H-21), 8.40 (d, *J* = 5.6 Hz, 1H, H-12), 8.28 (t, *J* = 7.2 Hz, 2H, H-12, H-16), 8.09 (s, 1H, H-17), 7.92–7.94 (m, 2H, H-1, H-4), 7.87 (s, 2H, H-2, H-3), 7.79–7.88 (m, 2H, H-23, H-14), 7.74 (t, *J* = 6.8 Hz, 1H, H-18), 6.63–6.77 (m, 2H, H-9), 6.33 (s, 2H, H-10), 6.15–6.19 (m, 2H, H-c, H-d), 6.05 (d, *J* = 5.6 Hz, 1H, H-e), 5.88 (d, *J* = 5.6 Hz, 1H, H-j), 2.64–2.67 (m, 1H, H-8), 2.18 (s, 3H, H-a), 1.08 (d, *J* = 6.8 Hz, 3H, H-i), 1.01 (d, *J* = 6.8 Hz, 3H, H-j). ¹⁹F NMR (DMSO-*d*₆, 376 MHz): δ –71.04 (PF₆), –69.15 (PF₆). ³¹P NMR (DMSO-*d*₆, 162 MHz): δ –152.98 (PF₆), –153.00 (PF₆), –148.61 (PF₆), –144.22 (PF₆), –139.83 (PF₆), –135.44 (PF₆). IR (cm^{–1}, KBr): 3082 (arm C–H stretching), 1450 (arm C=C stretching), 1280 (C–N stretching), 837 (P–F stretching), 781 (C–H bending). ESI-MS (MeOH): m/z : 717.6 [M]⁺. HRMS (MeOH): C₃₄H₃₂N₁₀ClF₆PRu (M) calculated m/z , 717.1543 [M – PF₆]⁺; observed m/z , 717.1552.

Synthesis of [(η⁵-Cp*)Ir^{III}Cl(K²-N,N-L)]PF₆ ([IrL]). First, 25 mg (0.031 mmol, 0.5 equiv) of [(η⁵-Cp*)IrCl(μ-Cl)]₂ was dissolved in 5

mL of methanol and stirred for 10 min to dissolve the compound completely in methanol. Then 1.1 equiv (29.4 mg) of previously prepared ligand (L) was added to the reaction mixture. The mixture was sonicated for 2 h at ambient temperature. When a change in color from orange to light yellow was observed, 1.1 equiv of NH₄PF₆ was added to the reaction mixture and stirred for another 2 h. The reaction was monitored by TLC using 100% methanol as solvent system. After the complete conversion, methanol was evaporated to dryness in air. To remove the impurities, crude product was washed thoroughly with 5 mL of hexane and dried. The purified product was further crystallized from methanol/diethyl ether mixture. The brown fine crystals were obtained with 90–95% yield. The structure of [IrL] was confirmed by ¹H, ¹⁹F, and ³¹P NMR, FT-IR, and ESI-MS. Purity of the complex was determined by HRMS analysis.

[(η⁵-Cp*)Ir^{III}Cl(K²-N,N-L)]PF₆ ([IrL]). Yield: 58 mg (0.060 mmol, 97%). *M_r* (C₃₄H₃₃N₁₀ClF₆PIr) = 954.33 g/mol. Anal. Calcd for C₃₄H₃₃N₁₀ClF₆PIr: C, 42.79; H, 3.49; N, 14.68. Found: C, 42.97; H, 3.25; N, 14.34. Yield: 97%. Mp: 170–172°C. *R_f* (100% methanol): 0.30. ¹H NMR (DMSO-*d*₆, 400 MHz): δ 9.47 (d, *J* = 6.4 Hz, 1H, H-19), 9.4 (d, *J* = 10.4 Hz, 1H, H-24), 8.97–9.01 (m, 2H, H-12, H-21), 8.56 (d, *J* = 7.6 Hz, 1H, H-22), 8.47 (d, *J* = 6.4 Hz, 1H, H-16), 8.27–8.35 (m, 2H, H-1, H-17), 7.81 (brs, 4H, H-2, H-3, H-4, H-14), 7.73–7.78 (m, 2H, H-18, H-23), 6.67–6.72 (m, 2H, H-9), 6.38 (s, 2H, H-10), 1.73 (s, 15H, H-1', H-2', H-3', H-4', H-5'). ¹⁹F NMR (DMSO-*d*₆, 376 MHz): δ –71.05 (PF₆), –69.16 (PF₆). ³¹P NMR (DMSO-*d*₆, 162 MHz): δ –152.98 (PF₆), –152.99 (PF₆), –148.60 (PF₆), –144.21 (PF₆), –139.82 (PF₆), –135.43 (PF₆), –131.04 (PF₆). IR (cm^{–1}, KBr): 3128 (arm C–H stretching), 1450 (arm C=C stretching), 1261 (C–N stretching), 835 (P–F stretching), 777 (C–H bending). ESI-MS (MeOH): m/z : 810.1 [M – PF₆]⁺. HRMS (MeOH): C₃₄H₃₃N₁₀ClF₆PIr (M) calculated m/z , 809.2207 [M – PF₆]⁺; observed m/z , 809.2205 [M]⁺.

Synthesis of [(η⁶-*p*-cymene)(η⁵-Cp*)Ru^{II}Ir^{III}Cl₂(K²-N,N-L)](PF₆)₂ ([RuIrL]). First 25 mg (0.031 mmol, 0.5 equiv) of [(η⁵-Cp*)IrCl(μ-Cl)]₂ was dissolved in 5 mL of methanol and stirred for 10 min to dissolve the compound completely in methanol. Then 1.1 equiv of previously prepared complex [RuL] was added to the reaction mixture. The mixture was sonicated for 2 h at ambient temperature. As soon as a change in color from orange to deep red was observed, 1.1 equiv of NH₄PF₆ was added to the reaction mixture and stirred for another 2 h to complete the reaction. The reaction was monitored by TLC using 100% methanol as solvent system. After the completion of reaction, methanol was evaporated. The impurities were removed by washing the crude product thoroughly with 5 mL of hexane followed by diethyl ether. The purified product was further crystallized from methanol/diethyl ether and the brown colored fine crystals of compound [RuIrL] was obtained with 95% yield. The structure of [RuIrL] were analyzed by ¹H, ¹⁹F, ¹³C, and ³¹P NMR, FT-IR, and ESI-MS. Purity of the complex was determined by C, H, N analysis and HRMS.

[(η⁶-*p*-cymene)(η⁵-Cp*)Ru^{II}Ir^{III}Cl₂(K²-N,N-L)](PF₆)₂ [RuIrL]. Yield: 82 mg (0.059 mmol, 95%). *M_r* (C₄₄H₄₇N₁₀Cl₂F₁₂P₂IrRu) = 1370.03 g/mol. Anal. Calcd for C₄₄H₄₇N₁₀Cl₂F₁₂P₂IrRu: C, 38.57; H, 3.46; N, 10.22. Found: C, 38.16; H, 3.31; N, 9.89. Yield: 98%. Mp: 185–187°C. *R_f* (100% methanol): 0.45. ¹H NMR (DMSO-*d*₆, 400 MHz): δ 9.53 (d, *J* = 5.2 Hz, 1H, H-19), 9.41–9.45 (m, 2H, H-1, H-4), 9.01 (d, *J* = 5.6 Hz, 1H, H-24), 8.55 (brs, 1H, H-12), 8.39 (brs, 1H, H-14), 8.26–8.34 (m, 2H, H-18, H-23), 7.78–7.83 (m, 4H, H-16, H-17, H-21, H-22), 7.72–7.76 (m, 2H, H-2, H-3), 6.70 (s, 4H, H-9, H-10), 6.15–6.19 (m, 2H, H-3, H-4), 6.04 (d, *J* = 6.0 Hz, 1H, H-5), 5.87 (d, *J* = 5.6 Hz, 1H, H-6), 2.62–2.67 (m, 1H, *p*-cymene, H-8), 2.18 (s, 3H, *p*-cymene, H-1), 1.73 (s, 15H, Cp*, H-6, H-7, H-8, H-9, H-10), 1.08 (d, *J* = 6.8 Hz, 3H *p*-cymene, H-9), 1.01 (d, *J* = 6.8 Hz, 3H, *p*-cymene, H-10). ¹³C NMR (DMSO-*d*₆, 100 MHz): δ 168.5 (2C, C-7, C-8), 162.9 (2C, C-15, C-20), 152.9 (2CH, C-19, C-24), 148.0 (2C, C-5, C-6), 140.6 (2CH, C-17, C-22), 131.6 (2C, C-11, C-13), 129.0 (2CH, C-12, C-14), 128.2 (2CH, C-1, C-4), 120.4 (2CH, C-2, C-3), 119.3 (2CH, C-16, C-21), 112.2 (2CH, C-18, C-23), {98.6, 92.6} (Cp*, 5C, C-1, C-2, C-3, C-4, C-5), {89.8, 89.4, 85.9, 81.3} (*p*-cymene, Ar–CH, C-3, C-4, C-5, C-6), 65.4 (CH₂, C-9, C-10), {22.9,

20.9) (*p*-cymene, isopropyl-CH₃, C-9, C-10), 19.2 (*p*-cymene, CH₃, C-1), {9.1, 8.8, 8.7} (Cp*, CH₃, C-6, C-7, C-8, C-9, C-10). ¹⁹F NMR (DMSO-*d*₆, 376 MHz): δ -71.06 (PF₆), -69.17 (PF₆). ³¹P NMR (DMSO-*d*₆, 162 MHz): δ -152.98 (PF₆), -153.00 (PF₆), -148.61 (PF₆), -144.22 (PF₆), -139.83 (PF₆), -135.44 (PF₆). IR (cm⁻¹, KBr): 3151 (arm C–H stretching), 1409 (arm C=C stretching), 833 (P–F stretching), 775.38 (C–H bending). ESI-MS (MeOH): *m/z*: 539.8 [M - 2PF₆]²⁺. HRMS (MeOH): C₄₄H₄₇N₁₀Cl₂F₁₂P₂IrRu (M) calculated *m/z*, 540.1017 [M - 2PF₆]²⁺, 1371.1397 [M + H]⁺; observed *m/z*, 540.1012[M - 2PF₆]²⁺, 1371.1398 [M + H]⁺.

■ ASSOCIATED CONTENT

■ Supporting Information

The Supporting Information is available free of charge at <https://pubs.acs.org/doi/10.1021/acs.inorgchem.0c02928>.

¹H, ³¹P, and ¹⁹F NMR, LCMS, IR, UV, and fluorescence spectra of all compounds and additional experimental information (PDF)

■ AUTHOR INFORMATION

Corresponding Authors

Priyankar Paira – Department of Chemistry, School of advanced sciences, Vellore Institute of Technology, Vellore 632014, Tamilnadu, India; orcid.org/0000-0003-1698-4895; Email: priyankar.paira@vit.ac.in

Bipasha Bose – Department Stem Cells and Regenerative Medicine Centre, Institution Yenepoya Research Centre, Yenepoya University, Derlakatte, Mangalore 575018, Karnataka, India; Email: bipasha.bose@gmail.com

Authors

Nilmadhab Roy – Department of Chemistry, School of advanced sciences, Vellore Institute of Technology, Vellore 632014, Tamilnadu, India

Utsav Sen – Department Stem Cells and Regenerative Medicine Centre, Institution Yenepoya Research Centre, Yenepoya University, Derlakatte, Mangalore 575018, Karnataka, India

Yukti Madaan – Department of Chemistry, School of advanced sciences, Vellore Institute of Technology, Vellore 632014, Tamilnadu, India

Venkatesan Muthukumar – Department of Chemistry, School of advanced sciences, Vellore Institute of Technology, Vellore 632014, Tamilnadu, India

Seshu Varddhan – Department of Applied Chemistry, S. V. National Institute of Technology (SVNIT) Ichchanath, Surat, Gujrat 395007, India

Suban K. Sahoo – Department of Applied Chemistry, S. V. National Institute of Technology (SVNIT) Ichchanath, Surat, Gujrat 395007, India; orcid.org/0000-0003-1751-5310

Debashis Panda – Department of Basic Sciences and Humanities, Rajiv Gandhi Institute of Petroleum Technology, An Institution of National Importance, Jais, Amethi 229304, Uttar Pradesh, India; orcid.org/0000-0002-2333-3735

Complete contact information is available at:

<https://pubs.acs.org/doi/10.1021/acs.inorgchem.0c02928>

Author Contributions

¹N.R. and U.S. made an equal contribution.

Notes

The authors declare no competing financial interest.

■ ACKNOWLEDGMENTS

The authors are grateful to the Department of Science and Technology, Government of India, for supporting the work through a DST-EMR project grant (EMR/2017/000816). The authors are grateful to VIT University for providing VIT SEED funding. We also acknowledge Professor A. Senthil Kumar and his group for helping in the cyclic voltammetry study. We acknowledge DST, New Delhi, India, for the DST-FIST Project.

■ LIST OF ABBREVIATIONS

NMR:nuclear magnetic resonance
 LCMS:liquid chromatography mass spectrometry
 HRMS:high resolution mass spectrometry
 ppm:parts per million
 MLCT:metal ligand charge transfer
 MTT:3-(4, 5-dimethylthiazol-2-yl)-2,5-diphenyltetrazolium bromide
 GSH:glutathione
 TLC:thin layer chromatography
 s:singlet
 d:doublet
 brs:broad singlet
 t:triplet
 m:multiplet
 OD:optical density
 CT-DNA:calf-thymus DNA
 BSA:bovine serum albumin
 HSA:human serum albumin
 EtBr:ethidium bromide
 DFT:density functional theory
 K_b:intrinsic binding constant
 K_{sv}:Stern–Volmer quenching constant
 K_{app}:apparent binding constant
 K:overall binding constant

■ REFERENCES

- (1) *Global Cancer - Facts and Figures*; American Cancer Society: 2007; p 1.
- (2) Thun, M. J.; DeLancey, J. O.; Center, M. M.; Jemal, A.; Ward, E. M. The global burden of cancer: priorities for prevention. *Carcinogenesis* **2010**, *31*, 100–110.
- (3) Rosenberg, B.; Vancamp, L.; Trosko, J. E.; Mansour, V. H. Platinum Compounds: a New Class of Potent Antitumour Agents. *Nature* **1969**, *222*, 385.
- (4) Reedijk, J. Improved understanding in platinumantitumour chemistry. *Chem. Commun.* **1996**, 801–806.
- (5) Ohndorf, U. M.; Rould, M. A.; He, Q.; Pabo, C. O.; Lippard, S. J. Basis for Recognition of Cisplatin-Modified DNA by High-Mobility-Group Proteins. *Nature* **1999**, *399*, 708–712.
- (6) Borst, P.; Rottenberg, S.; Jonkers, J. How do real tumors become resistant to cisplatin? *Cell Cycle* **2008**, *7*, 1353–1359.
- (7) Barabas, K.; Milner, R.; Lurie, D.; Adin, C. Cisplatin: A review of toxicities and therapeutic applications. *Vet. Comp. Oncol.* **2008**, *6*, 1–18.
- (8) Allardyce, C. S.; Dyson, P. J. Ruthenium in Medicine: Current Clinical Uses and Future prospects. *Platinum Met. Rev.* **2001**, *45*, 62–69.
- (9) Podlech, J.; Maier, T. C. Indium in Organic Synthesis. *Synthesis* **2003**, 0633–0655.
- (10) Li, C. J.; Chan, T. H. Organometallic reactions in aqueous media with indium. *Tetrahedron Lett.* **1991**, *32*, 7017–7020.
- (11) Hartinger, C. G.; Zorbas-Seifried, S.; Jakupec, M. A.; Kynast, B.; Zorbas, H.; Keppler, B. K. From bench to bedside-preclinical and early clinical development of the anticancer agent indazolium trans-

[tetrachlorobis(1H-indazole)ruthenate(III)] (KP1019 or FFC14A). *J. Inorg. Biochem.* **2006**, *100*, 891–904.

(12) Rademaker-Lakhai, J. M.; Van Den Bongard, D.; Pluim, D.; Beijnen, J. H.; Schellens, J. H. M. A Phase I and Pharmacological Study with Imidazolium-trans-DMSO-imidazole-tetrachlororuthenate, a Novel Ruthenium Anticancer Agent. *Clin. Cancer Res.* **2004**, *10*, 3717–3727.

(13) Jakupec, M. A.; Arion, V. B.; Kapitzka, S.; Reisner, E.; Eichinger, A.; Pongratz, M.; Marian, B.; Graf v. Keyserlingk, N.; Keppler, B. K. KP1019 (FFC14A) from bench to bedside: preclinical and early clinical development—an overview. *Int. J. Clin. Pharmacol. Ther.* **2005**, *43*, 595–596.

(14) Levina, A.; Mitra, A.; Lay, P. A. Recent developments in ruthenium anticancer drugs. *Metallomics* **2009**, *1*, 458–470.

(15) Zeng, L.; Gupta, P.; Chen, Y.; Wang, E.; Ji, L.; Chao, H.; Chen, Z.-S. The development of anticancer ruthenium(II) complexes: from single molecule compounds to nanomaterials. *Chem. Soc. Rev.* **2017**, *46*, 5771–5804.

(16) (a) Smithen, D. A.; Yin, H.; Beh, M. H. R.; Hetu, M.; Cameron, T. S.; McFarland, S. A.; Thompson, A. Synthesis and Photobiological Activity of Ru(II) Dyads Derived from Pyrrole-2-carboxylate Thionoesters. *Inorg. Chem.* **2017**, *56*, 4121–4132. (b) Monro, S.; Colón, K. L.; Yin, H.; Roque, J., 3rd; Konda, P.; Gujar, S.; Thummel, R. P.; Lilje, L.; Cameron, C. G.; McFarland, S. A. Transition Metal Complexes and Photodynamic Therapy from a Tumor-Centered Approach: Challenges, Opportunities, and Highlights from the Development of TLD1433. *Chem. Rev.* **2019**, *119*, 797–828.

(17) Berndsen, R. H.; Weiss, A.; Abdul, U. K.; Wong, T. J.; Meraldi, P.; Griffioen, A. W.; Dyson, P. J.; Nowak-Sliwinska, P. Combination of ruthenium(II)-arene complex [Ru(η^6 -*p*-cymene)Cl₂(pta)] (RAPTA-C) and the epidermal growth factor receptor inhibitor erlotinib results in efficient angiostatic and antitumor activity. *Sci. Rep.* **2017**, *7*, 43005.

(18) Sadler, P. J.; Lainez, R. F.; Abraba, H.; Michael, M.; Duncan, J. M.; Ruthenium Anticancer Complexes. U.S. Patent US 20060058270 A1, Mar 16, 2006.

(19) Wenjie, M. Chair Ruthenium Complexes and Their Use as Anticancer Agents. U.S. Patent US 8,357,678 B2, Jan 22, 2013.

(20) Mestroni, G.; Alessio, E.; Sava, G.; New Salts of Anionic Complexes of Ru(III) as Antimetastatic and Antineoplastic Agents WO Patent WO1998000431A1, Jan 8, 1998.

(21) Gamble, A. J.; Lynam, J. M.; Walton, P. H.; Synthesis an Anticancer activity of Ruthenium(II) cis-cis-1,3,5-Triaminocyclohexane Complexes. WO Patent WO2013038134A1, Mar 21, 2013.

(22) Morris, R. E.; Sadler, P. J.; Chen, H.; Jodrell, D.; Half-Sandwich Ruthenium(II) Compounds Comprising Nitrogen Containing Ligands for Treatment of Cancer. U.S. Patent US 20050239765 A1, Dec 27, 2005.

(23) Morris, R. E.; Sadler, P. J.; Jodrell, D.; Chen, H.; Ruthenium(II) Compounds for Use in the Therapy of Cancer. U.S. Patent US 6,936,634 B2, Aug 30, 2005.

(24) Keppler, B. K.; Medicament Preparations Containing Tumor-Inhibiting Ruthenium(III) Complexes. WO Patent WO1997036595A3, Nov 6, 1997.

(25) Mestroni, G.; Alessio, E.; Sava, G.; Lengo, E.; Zorzet, S.; Bergamo, A. Ruthenium Dimeric Compounds Suitable as Antimetastatic and Antineoplastic Agents. U.S. Patent US 6,921,824 B1, Jul 26, 2005.

(26) Adhikarsan, Z.; Davey, G. E.; Campomanes, P.; Groessl, M.; Clavel, C. M.; Yu, H.; Nazarov, A. A.; Yeo, C. H.; Ang, W. H.; Droge, P.; Rothlisberger, U.; Dyson, P. J.; Davey, C. A. Combination of ruthenium(II)-arene complex [Ru(η^6 -*p*-cymene)Cl₂(pta)] (RAPTA-C) and the epidermal growth factor receptor inhibitor erlotinib results in efficient angiostatic and antitumor activity. *Nat. Commun.* **2014**, *5*, 3462.

(27) Debreczeni, J. É.; Bullock, A. N.; Atilla, G. E.; Williams, D. S.; Bregman, H.; Knapp, S.; Meggers, E. Ruthenium half-sandwich complexes bound to protein kinase Pim-1. *Angew. Chem., Int. Ed.* **2006**, *45*, 1580–1585.

(28) Chatterjee, S.; Kundu, S.; Bhattacharyya, A.; Hartinger, C. G.; Dyson, P. J. The ruthenium(II)-arene compound RAPTA-C induces apoptosis in EAC cells through mitochondrial and p53-JNK pathways. *J. Biol. Inorg. Chem.* **2008**, *13*, 1149–1155.

(29) Lee, R. F. S.; Escrig, S.; Maclachlan, C.; Knott, G. W.; Meibom, A.; Sava, G.; Dyson, P. J. The Differential Distribution of RAPTA-T in Non-Invasive and Invasive Breast Cancer Cells Correlates with Its Anti-Invasive and Anti-Metastatic Effects. *Int. J. Mol. Sci.* **2017**, *18*, 1869.

(30) Novohradsky, V.; Zerzankova, L.; Stepankova, J.; Kisova, A.; Kosthunova, H.; Liu, Z.; Sadler, P. J.; Kasparkova, J.; Brabec, V. A dual-targeting apoptosis inducing organometallic half-sandwich iridium anticancer complex. *Metallomics* **2014**, *6*, 1491–1501.

(31) Rangasamy, S.; Ju, H.; Um, S.; Oh, D.-C.; Song, J. M. Mitochondria and DNA Targeting of 5,10,15,20-Tetrakis(7-sulfonatobenzo[b]thiophene) Porphyrin-Induced Photodynamic Therapy via Intrinsic and Extrinsic Apoptotic Cell Death. *J. Med. Chem.* **2015**, *58*, 6864–6874.

(32) Zhang, C.; Qiu, K.; Liu, C.; Huang, H.; Rees, T. W.; Ji, L.; Zhang, Q.; Chao, H. Tracking mitochondrial dynamics during apoptosis with phosphorescent fluorinated iridium(III) complexes. *Dalton Trans.* **2018**, *47*, 12907–12913.

(33) Singh, D. P.; Deivedi, S. K.; Hashim, S. R.; Singhal, R. G. Synthesis and Antimicrobial Activity of some New Quinoxaline Derivatives. *Pharmaceuticals* **2010**, *3*, 2416–2425.

(34) Rong, F.; Chow, S.; Yan, S.; Larson, G.; Hong, Z.; Wu, J. Structure-activity relationship (SAR) studies of quinoxalines as novel HCV NSSB RNA-dependent RNA polymerase inhibitors. *Bioorg. Med. Chem. Lett.* **2007**, *17*, 1663–1666.

(35) Jaso, A.; Zarranz, B.; Aldana, I.; Monge, A. Synthesis of New Quinoxaline-2-carboxylate 1,4-Dioxide derivatives as Anti-Mycobacterium tuberculosis Agents. *J. Med. Chem.* **2005**, *48*, 2019–2025.

(36) Smits, R. A.; Lim, H. D.; Hanzer, A.; Zuiderveld, O. P.; Guaita, E.; Adami, M.; Coruzzi, G.; Leurs, R.; de Esch, I. J. P. Discovery of Quinoxalines as Histamine H₄ Receptor Inverse Agonists Using a Scaffold Hopping Approach. *J. Med. Chem.* **2008**, *51*, 2457–2467.

(37) Burguete, A.; Pontiki, E.; Hadjipavlou-Litina, D.; Villar, R.; Vicente, E.; Solano, B.; Ancizu, S.; Perez-Silanes, S.; Aldana, I.; Monge, A. Synthesis and anti-inflammatory/antioxidant activities of some new ring substituted 3-phenyl-1-(1,4-di-N-oxide quinoxalin-2-yl)-2-propen-1-one derivatives and of their 4,5-dihydro-(1H)-pyrazole analogues. *Bioorg. Med. Chem. Lett.* **2007**, *17*, 6439–6443.

(38) Naylor, M. A.; Stephen, M. A.; Nolan, J.; Sutton, B.; Tochcer, J. H.; Fielden, E. M.; Adams, G. E.; Strafford, I. J. Heterocyclic mono-N-oxides with potential applications as bioreductive anti-tumour drugs: Part 1. 8-Alkylamino-substituted phenylimidazo [1, 2-a] quinoxalines. *Anticancer Drug Res.* **1993**, *8*, 439–461.

(39) Gil, M. V.; Arevalo, M. J.; Lopez, O. Click Chemistry what's in a Name? Triazole Synthesis and Beyond. *Synthesis* **2007**, *2007*, 1589.

(40) Binder, W. H.; Kluger, C. Azide/Alkyne “Click” Reactions: Applications in Material Science and Organic Synthesis. *Curr. Org. Chem.* **2006**, *10*, 1791–1815.

(41) Lutz, J. F. I, 3-Dipolar Cycloadditions of Azides and Alkynes: A Universal Ligation Tool in Polymer and Material Science. *Angew. Chem., Int. Ed.* **2007**, *46*, 1018–1025.

(42) Binder, W. H.; Sachsenhofer, R. ‘Click’ Chemistry in Polymer and Materials Science. *Macromol. Rapid Commun.* **2007**, *28*, 15–54.

(43) Hawker, C. J.; Wooley, K. L. The convergence of synthetic organic and polymer chemistries. *Science* **2005**, *309*, 1200–1205.

(44) Read, E. S.; Armes, S. P. Recent advances in shell cross-linked micelles, Recent advances in shell cross-linked micelles. *Chem. Commun.* **2007**, 3021–3035.

(45) Singhal, N.; Sharma, P. K.; Dudhe, R.; Kumar, N. Recent advancement of triazole derivatives and their biological significance. *J. Chem. Pharm. Res.* **2011**, *3*, 120–126.

(46) Amr, A. E.; Sabry, N. M.; Abdulla, M. M. Synthesis, Reactions, and Anti-inflammatory Activity of Heterocyclic Systems Fused to a Thiophene Moiety Using Citrazinic Acid As Synthone. *Monatsh. Chem.* **2007**, *138*, 699–707.

- (47) Fujiwara, N.; Nakajima, T.; Ueda, Y.; Fujita, H.; Kawakami, H. Novel piperidinylpyrimidine derivatives as inhibitors of HIV-1 LTR activation. *Bioorg. Med. Chem.* **2008**, *16*, 9804–9816.
- (48) Thirumurugan, P.; Matosiuk, D.; Jozwiak, K. Click Chemistry for Drug Development and Diverse Chemical–Biology Applications. *Chem. Rev.* **2013**, *113*, 4905–4979.
- (49) Maiti, S.; Roy, N.; Babu, L. T.; Moharana, P.; Athira, C. C.; Darsana Sreedhar, E.; De, S.; Ashok Kumar, S. K.; Paira, P. Cu(ii), Ir(i) and CuOnanocatalyzed mild synthesis of luminescent symmetrical and unsymmetrical bis(triazolylmethyl)quinoxalines: biocompatibility, cytotoxicity, live cell imaging and biomolecular interaction. *New J. Chem.* **2020**, *44*, 920–931.
- (50) Chen, Y.; Qiao, L.; Ji, L.; Chao, H. Phosphorescent iridium(III) complexes as multicolor probes for specific mitochondrial imaging and tracking. *Biomaterials* **2014**, *35*, 2–13.
- (51) Jin, C.; Liu, J.; Chen, Y.; Zeng, L.; Guan, R.; Ouyang, C.; Ji, L.; Chao, H. Cyclometalated Iridium(III) Complexes as Two-Photon Phosphorescent Probes for Specific Mitochondrial Dynamics Tracking in Living Cells. *Chem. - Eur. J.* **2015**, *21*, 12000–12010.
- (52) Kubanik, M.; Holtkamp, H.; Söhnel, T.; Jamieson, S. M. F.; Hartinger, C. G. Impact of the Halogen Substitution Pattern on the Biological Activity of Organoruthenium 8-Hydroxyquinoline Anticancer Agents. *Organometallics* **2015**, *34*, 5658–5668.
- (53) Gilewska, A.; Barszcz, B.; Masternak, J.; Kazimierzczuk, K.; Sitkowski, J.; Wietrzyk, J.; Turlej, E. Similarities and differences in d^6 low-spin ruthenium, rhodium and iridium half-sandwich complexes: synthesis, structure, cytotoxicity and interaction with biological targets JBIC. *J. Biol. Inorg. Chem.* **2019**, *24*, 591–606.
- (54) Aman, F.; Hanif, M.; Siddiqui, W. A.; Ashraf, A.; Filak, L. K.; Reynisson, J.; Söhnel, T.; Jamieson, S. M.; Hartinger, C. G. Anticancer Ruthenium(η^6 -*p*-cymene) Complexes of Nonsteroidal Anti-inflammatory Drug Derivatives. *Organometallics* **2014**, *33*, 5546–5553.
- (55) (a) Geary, W. J. The use of conductivity measurements in organic solvents for the characterization of coordination compounds. *Coord. Chem. Rev.* **1971**, *7*, 81–122. (b) Ali, I.; Wani, W. A.; Saleem, K. Empirical Formulae to Molecular Structures of Metal Complexes by Molar Conductance, Synthesis and Reactivity in Inorganic. *Synth. React. Inorg., Met.-Org., Nano-Met. Chem.* **2013**, *43*, 1162–1170. (c) Banerjee, S.; Pant, I.; Khan, I.; Prasad, P.; Hussain, A.; Kondaiah, P.; Chakravarty, A. R. Remarkable enhancement in photocytotoxicity and hydrolytic stability of curcumin on binding to an oxovanadium(IV) moiety. *Dalton Trans.* **2015**, *44*, 4108–4122.
- (56) (a) Díez, J.; Gimeno, J.; Lledós, A.; Suárez, F. J.; Vicent, C. Imidazole Based Ruthenium(IV) Complexes as Highly Efficient Bifunctional Catalysts for the Redox Isomerization of Allylic Alcohols in Aqueous Medium: Water as Cooperating Ligand. *ACS Catal.* **2012**, *2*, 2087–2099. (b) Romero-Canelón, I.; Sadler, P. J. Next-Generation Metal Anticancer Complexes: Multitargeting via Redox Modulation. *Inorg. Chem.* **2013**, *52*, 12276–12291.
- (57) Townsend, D. M.; Tew, K. D. The role of glutathione-S-transferase in anti-cancer drug resistance. *Oncogene* **2003**, *22*, 7369–7375.
- (58) Campling, B. G.; Baer, K.; Baker, H. M.; Lam, Y. M.; Cole, S. P. Do glutathione and related enzymes play a role in drug resistance in small cell lung cancer cell lines? *Br. J. Cancer* **1993**, *68*, 327–335.
- (59) Seršen, S.; Kljun, J.; Kryeziu, K.; Panchuk, R.; Alte, B.; Körner, W.; Heffeter, P.; Berger, W.; Turel, I. Structure-Related Mode-of-Action Differences of Anticancer Organoruthenium Complexes with β -Diketones. *J. Med. Chem.* **2015**, *58*, 3984–3996.
- (60) Gamcsik, M. P.; Kasibhatla, M. S.; Teeter, S. D.; Colvin, O. M. Glutathione levels in human tumors. *Biomarkers* **2012**, *17*, 671–691.
- (61) Saravanan, N.; Gandhi, M.; Senthil Kumar, A. High-valent ruthenium(IV)-oxo complex stabilized mesoporous carbon (graphitized)/nafion modified electrocatalyst for methanol oxidation reaction in neutral pH. *J. Electroanal. Chem.* **2020**, *874*, 114457.
- (62) Frisch, M. J.; Trucks, G. W.; Schlegel, H. B.; Scuseria, G. E.; Robb, M. A.; Cheeseman, J. R.; Farkas, A. D.; Foresman, J. B.; Ortiz, J. V.; Cioslowski, J.; Fox, D. J. Gaussian 09W; Gaussian, Inc., Wallingford, CT, 2009.
- (63) Morris, G. M.; Huey, R.; Lindstrom, W.; Sanner, M. F.; Belew, R. K.; Goodsell, D. S.; Olson, A. J. AutoDock4 and AutoDockTools4: Automated docking with selective receptor flexibility. *J. Comput. Chem.* **2009**, *30* (16), 2785–2791.
- (64) Liu, P.; Wu, B.; Liu, J.; Dai, Y.; Wang, Y.; Wang, K. DNA Binding and Photocleavage Properties, Cellular Uptake and Localization, and in-Vitro Cytotoxicity of Dinuclear Ruthenium(II) Complexes with Varying Lengths in Bridging Alkyl Linkers. *Inorg. Chem.* **2016**, *55*, 1412–1422.
- (65) (a) Liu, Z.-C.; Wang, B.-D.; Yang, Z.-Y.; Li, Y.; Qin, D.-D.; Li, T.-R. Synthesis, crystal structure, DNA interaction and antioxidant activities of two novel water-soluble Cu^{2+} complexes derived from 2-oxo-quinoline-3-carbaldehyde Schiff-bases. *Eur. J. Med. Chem.* **2009**, *44*, 4477–4484. (b) Herebian, D.; Sheldrick, W. S. Synthesis and DNA binding properties of bioorganometallic (η^5 -pentamethylcyclopentadienyl)iridium(III) complexes of the type $[(\eta^5-C_5Me_5)Ir(Aa)(dppz)]^{n+}$ ($dppz = dipyrido[3,2-a:2',3'-c]$ -phenazine, $n = 1-3$), with S-coordinated amino acids (Aa) or peptides. *J. Chem. Soc., Dalton Trans.* **2002**, 966–974. (c) Grover, N.; Welch, T. W.; Fairley, T. A.; Cory, M.; Thorp, H. H. Oxidation of DNA by trans-dioxoruthenium(VI) complexes: self-inhibition of DNA cleavage by metal complexes. *Inorg. Chem.* **1994**, *33*, 3544–3548. (d) Sarkar, B.; Mondal, A.; Madaan, Y.; Roy, N.; Moorthy, A.; Kuo, Y.-C.; Paira, P. Luminescent anticancer ruthenium(II)-*p*-cymene complexes of extended imidazophenanthroline ligands: synthesis, structure, reactivity, biomolecular interactions and live cell imaging. *Dalton Transaction* **2019**, *48*, 12257–12271. (e) P.K., A.; Paira, P. Luminescent anticancer Ru(II)-arenebipyridine and phenanthroline complexes: Synthesis, characterization, DFT studies, biological interactions and cellular imaging application. *J. Inorg. Biochem.* **2020**, *208*, 111099. (f) Mondal, A.; Paira, P. Hypoxia efficient and glutathione-resistant cytospecific ruthenium (II)-*p*-cymene-arylimidazophenanthroline complexes: biomolecular interaction and live cell imaging. *Dalton Transactions* **2020**, *49*, 12865–12878. (g) Khan, T. A.; Bhar, K.; Thirumoorthi, R.; Roy, T. K.; Sharma, A. K. Design, synthesis, characterization and evaluation of the anticancer activity of water-soluble halfsandwichruthenium(II) arenehalido complexes. *New J. Chem.* **2020**, *44*, 239.
- (66) (a) Zhen, Q. X.; Ye, B. H.; Zhang, Q. L.; Liu, J. G.; Li, H.; Ji, L. N.; Wang, L. Synthesis, characterization and the effect of ligand planarity of $[Ru(bpy)_2L]^{2+}$ on DNA binding affinity. *J. Inorg. Biochem.* **1999**, *76*, 47–53. (b) Pyle, A. M.; Rehmann, J. P.; Meshoyrer, R.; Kumar, C. V.; Turro, N. J.; Barton, J. K. Mixed-ligand complexes of ruthenium(II): factors governing binding to DNA. *J. Am. Chem. Soc.* **1989**, *111*, 3051–3058.
- (67) (a) Chen, H.; Parkinson, J. A.; Morris, R. E.; Sadler, P. J. Highly Selective Binding of Organometallic Ruthenium Ethylenediamine Complexes to Nucleic Acids: Novel Recognition Mechanisms. *J. Am. Chem. Soc.* **2003**, *125*, 173–186. (b) Dimiza, F.; Perdih, F.; Tangoulis, V.; Turel, I.; Kessissoglou, D. P.; Psomas, G. Interaction of copper(II) with the non-steroidal anti-inflammatory drugs naproxen and diclofenac: synthesis, structure, DNA- and albumin-binding. *J. Inorg. Biochem.* **2011**, *105*, 476–489.
- (68) Van Niekerk, A.; Chellan, P.; Mapolie, S. F. Heterometallic Multinuclear Complexes as Anti-Cancer Agents-An Overview of Recent Developments. *Eur. J. Inorg. Chem.* **2019**, *2019*, 3432–3455.
- (69) Sen, U.; Shenoy P, S.; Bose, B. Opposing effects of low versus high concentrations of water soluble vitamins/dietary ingredients Vitamin C and niacin on colon cancer stem cells (CSCs). *Cell Biol. Int.* **2017**, *41*, 1127–1145.